

The age of the Galactic thin disk from Th/Eu nucleocosmochronology

I. Determination of [Th/Eu] abundance ratios*

E.F. del Peloso¹, L. da Silva¹, and G.F. Porto de Mello²

¹ Observatório Nacional/MCT, Rua General José Cristino 77, 20921-400 Rio de Janeiro, Brazil
e-mail: epeloso@on.br, licio@on.br

² Observatório do Valongo/UFRJ, Ladeira do Pedro Antônio 43, 20080-090 Rio de Janeiro, Brazil
e-mail: gustavo@ov.ufrj.br

Received \mid date \mid / Accepted \mid date \mid

Abstract. The purpose of this work is to resume investigation of Galactic *thin disk* dating using nucleocosmochronology with Th/Eu stellar abundance ratios, a theme absent from the literature since 1990. A stellar sample of 20 disk dwarfs/subgiants of F5 to G8 spectral types with $-0.8 \leq [\text{Fe}/\text{H}] \leq +0.3$ was selected. In stars with such spectral types and luminosity classes, spectral synthesis techniques must be employed if we wish to achieve acceptably accurate results. An homogeneous, self-consistent set of atmospheric parameters was determined. Effective temperatures were determined from photometric calibrations and H α profile fitting; surface gravities were obtained from T_{eff} , stellar masses and luminosities; microturbulence velocities and metallicities were obtained from detailed, differential spectroscopic analysis, relative to the Sun, using equivalent widths of Fe I and Fe II lines. Chemical abundances of the elements that contaminate the Th and Eu spectral regions (Ti, V, Cr, Mn, Co, Ni, Ce, Nd, and Sm) were determined through spectroscopic analysis. Abundance uncertainties were thoroughly scrutinised, their average value $-(0.10 \pm 0.02)$ dex – being found to be satisfactorily low. Eu and Th abundances were determined by spectral synthesis of one Eu II line (4129.72 Å) and one Th II line (4019.13 Å), taking into account the detailed hyperfine structures of contaminating Co lines, as well as the hyperfine structure and isotope shift of the Eu line. Comparison of our abundances with literature data shows that our results exhibit a similar behaviour, but a considerably lower scatter (36% lower for Eu, and 61% lower for Th). The [Th/Eu] abundance ratios thus obtained were used, in the second paper of this series, to determine the age of the Galactic disk.

Key words. Galaxy: disk – Galaxy: evolution – Stars: late-type – Stars: fundamental parameters – Stars: abundances

1. Introduction

Modern methods of estimating the age of the Galactic thin disk¹, like dating the oldest open clusters by isochrone fitting and white dwarfs by cooling sequences, rely heavily on stellar evolution calculations. Nucleocosmochronology is a dating method that makes use of only a few results of main sequence stellar evolution models, therefore allowing a quasi-independent verification of the afore-mentioned techniques.

Nucleocosmochronology employs the abundances of radioactive nuclides to determine timescales for astrophysical ob-

jects and events. The Th/Eu chronometer was first proposed by Pagel (1989) as a way of assessing the age of the Galactic disk. Its main advantages are that ^{232}Th has a 14.05 Gyr half-life, i.e., of the order of magnitude of the age being assessed, and that Eu provides a satisfactory element for comparison, being produced almost exclusively (97%, according to Burris et al. 2000) by the same nucleosynthetic process that produces all Th, the r-process. Its main disadvantage lies in the difficulty one encounters when trying to determine stellar Th abundances. This difficulty arises from the very low equivalent width (EW) of the Th II line used, and from the fact that it is severely blended with other much stronger lines.

The first to suggest the presence of a Th II line in the solar spectrum, located at 4019.137 Å, were Sitterly & King (1943). Severny (1958) was the first to measure the EW of this line, deriving an upper limit for the solar thorium abundance. The first confirmed Th detection and abundance determination in a star other than the Sun was accomplished by Cowley et al. (1975)

Send offprint requests to: E.F. del Peloso

* Based on observations collected at the European Southern Observatory, La Silla, Chile, under the ESO programs and the ESO-Observatório Nacional, Brazil, agreement, and at the Observatório do Pico dos Dias, operated by the Laboratório Nacional de Astrofísica/MCT, Brazil.

¹ All references to the *Galactic disk* must be regarded, in this work, as references to the *thin disk*, unless otherwise specified.

in HR 465, an Ap star. Until today, only two works available in the literature have presented Th abundances for samples of Galactic disk stars: da Silva et al. (1990) and Morell et al. (1992, MKB92). Of these, only da Silva et al. present a chronological analysis.

This project aims at resuming investigation of Galactic disk dating using [Th/Eu] abundance ratios, a theme absent from the literature since 1990.² In this paper, Part I of a series, we carried out the preliminary, observationally-oriented steps required. First, an appropriate stellar sample had to be elected. Selection considered the suitability of the sample to the task of Galactic *disk* dating, with criteria like metallicity and spectral type range. In stars with spectral types and luminosity classes adequate to our study, which are F5–K2 dwarfs and subgiants (see Sect. 2.1), there are only one Th and one Eu line adequate for abundance determinations. This means that spectral synthesis techniques had to be called upon so as to obtain acceptably accurate results. As prerequisites to the synthesis, we determined accurate atmospheric parameters and chemical abundances of the elements that contaminate the Th and Eu spectral regions (Ti, V, Cr, Mn, Co, Ni, Ce, Nd, and Sm). Eu and Th abundances were determined for all sample stars by spectral synthesis, using our atmospheric parameters and abundances. The [Th/Eu] abundance ratios thus obtained were used, in the second paper of this series (del Peloso et al. 2005a, Paper II), to determine the age of the Galactic disk.

2. Sample selection, observations, and data reduction

The stellar sample was defined using the Hipparcos catalogue (Perryman & ESA 1997), upon which a series of selection criteria were applied. All objects in the final sample were observed with the Fiber-fed Extended Range Optical Spectrograph (FEROS; Kaufer et al. 1999) fed by the 1.52 m European Southern Observatory (ESO) telescope, in the ESO–Observatório Nacional, Brazil, agreement. Spectra were also obtained with a coudé spectrograph fed by the 1.60 m telescope of the Observatório do Pico dos Dias (OPD), LNA/MCT, Brazil, and with the Coudé Échelle Spectrometer (CES) fiber-fed by ESO’s 3.60 m telescope and Coudé Auxiliary Telescope (CAT). The selection criteria are related in detail below, followed by the description of the observations and their reduction.

2.1. Selection criteria

Multiple criteria were applied to the Hipparcos catalogue, composed of 118 218 objects. Initially, we eliminated objects with parallaxes lower than $0.010''$, in order to insure minimum uncertainty in the derived bolometric magnitudes (22 982 objects left). Only stars with declination $\delta \leq +20^\circ$ were kept, to

² In this paper we obey the following customary spectroscopic notations: absolute abundance $\log \varepsilon(A) \equiv \log_{10}(N_A/N_H) + 12.0$, and abundance ratio $[A/B] \equiv \log_{10}(N_A/N_B)_{\text{star}} - \log_{10}(N_A/N_B)_{\odot}$, where N_A and N_B are the abundances of elements A and B, respectively, in atoms cm^{-3} .

allow the observations to be carried out in the southern hemisphere (15 898 objects left). Stars fainter than visual magnitude $V = 7.0$ were removed, so that high resolution, high S/N ratio spectra could be obtained with relatively short total exposures (i.e., less than 3 hours in total) on small and medium sized telescopes (3272 objects left).

The subsequent criteria aimed at constructing the most suitable sample for Galactic disk nucleocosmochronology. Spectral types were restricted to the F5–K2 range because these stars have life-times comparable to the age of the Galaxy (1744 objects left). Only luminosity classes IV and V were allowed, to avoid stars whose photospheric abundances had been altered by dredge-up episodes, and to minimise non-LTE effects (925 objects left). Since spectral analysis would be differential, we limited the sample to stars with atmospheric parameters similar to the Sun by selecting objects with a (B–V) color index in the interval $[+0.45, +0.82]$, so that their effective temperatures fell in the range $T_{\text{eff}} \pm 400$ (744 objects left). As the ultimate objective of this work is the determination of the age of the Galactic *disk*, we eliminated stars with $[\text{Fe}/\text{H}] < -1.00$ (252 objects left); for this purpose, we employed average metallicities from the catalogue of Cayrel de Strobel et al. (2001).

Stars listed as double in the Bright Star (Warren & Hoffleit 1987) or Hipparcos catalogues were rejected. As a last criterium, we only kept stars whose masses could be determined with the Geneva sets of evolutionary tracks (Schaller et al. 1992, Charbonnel et al. 1993, Schaerer et al. 1993a,b, and Charbonnel et al. 1996, hereafter collectively referred to as Gen92/96). For this purpose, stars were required to be located between tracks in at least two of the HR diagrams constructed for different metallicities. This left 157 objects in the sample.

To reach a suitably sized sample, we kept only the brightest stars to end up with 2 to 4 objects per 0.25 dex metallicity bin in the interval $-1.00 \leq [\text{Fe}/\text{H}] \leq +0.50$, and a total of 20 dwarfs and subgiants of F5 to G8 spectral type (Table 1).

2.2. Checks of sample contamination

Our sample is restricted to objects closer than 40 pc. It is a very localised sample, considering that the Galactic thin disk has a 290 pc scale height (Buser et al. 1998). This greatly reduces the probability of halo stars contaminating our sample, because the local density of halo stars is less than 0.05% (Buser et al. 1998). In order to reduce even further the probability of contamination, we restricted our sample to relatively high metallicities ($[\text{Fe}/\text{H}] \geq -1.00$). However, these criteria are not perfect, because there exists an intersection between the metallicity distributions of disk and halo stars, i.e., there exists a non-negligible, albeit small, number of halo stars with $[\text{Fe}/\text{H}] \geq -1.00$. As an additional check of contamination, we performed a kinematic analysis of the objects.

We developed a code to calculate the U, V, and W spatial velocity components. This code is based on the Johnson & Soderblom (1987) formulation and makes use of the Perryman et al. (1998) coordinate transformation matrix. It calculates the velocity components relative to the Sun, and

Table 1. Selected stellar sample.

HD	HR	HIP	Name	R.A.	DEC	Parallax	V	Spectral type and luminosity class
				2000.0 (h m s)	2000.0 (d m s)	(mas)		
2151	98	2021	β Hyi	00 25 45	-77 15 15	133.78	2.80	G1 IV
9562	448	7276	-	01 33 43	-07 01 31	33.71	5.76	G3 V
16 417	772	12 186	λ^2 For	02 36 59	-34 34 41	39.16	5.78	G1 V
20 766	1006	15 330	ζ^1 Ret	03 17 46	-62 34 31	82.51	5.54	G3-5 V
20 807	1010	15 371	ζ^2 Ret	03 18 13	-62 30 23	82.79	5.24	G2 V
22 484	1101	16 852	10 Tau	03 36 52	+00 24 06	72.89	4.28	F8 V
22 879	-	17 417	-	03 40 22	-03 13 01	41.07	6.74	F7-8 V
30 562	1536	22 336	-	04 48 36	-05 40 27	37.73	5.77	G5 V
43 947	-	30 067	-	06 19 40	+16 00 48	36.32	6.63	F8 V
52 298	-	33 495	-	06 57 45	-52 38 55	27.38	6.94	F5-6 V
59 984	2883	36 640	-	07 32 06	-08 52 53	33.40	5.93	G5-8 V
63 077	3018	37 853	171 Pup	07 45 35	-34 10 21	65.79	5.37	G0 V
76 932	3578	44 075	-	08 58 44	-16 07 58	46.90	5.86	F7-8 IV-V
102 365	4523	57 443	-	11 46 31	-40 30 01	108.23	4.91	G3-5 V
128 620	5459	71 683	α Cen A	14 39 37	-60 50 02	742.12	-0.01	G2 V
131 117	5542	72 772	-	14 52 33	-30 34 38	24.99	6.29	G0-1 V
160 691	6585	86 796	μ Ara	17 44 09	-51 50 03	65.46	5.15	G3 IV-V
196 378	7875	101 983	ϕ^2 Pav	20 40 03	-60 32 56	41.33	5.12	F7 V
199 288	-	103 458	-	20 57 40	-44 07 46	46.26	6.52	G0 V
203 608	8181	105 858	γ Pav	21 26 27	-65 21 58	108.50	4.22	F7 V

References: Coordinates: SIMBAD (FK5 system); parallaxes: Hipparcos catalogue (Perryman & ESA 1997); visual magnitudes: Bright Star Catalogue (Warren & Hoffleit 1987) for stars with an HR number and SIMBAD for those without; spectral types and luminosity classes: Michigan Catalogue of HD Stars (Houk & Cowley 1975; Houk 1978, 1982; Houk & Smith-Moore 1988; Houk & Swift 1999) for all stars, with the exception of HD 182 572 and HD 196 755 (Bright Star Catalogue), and HD 43 047 (Fehrenbach 1961).

then converts them to the local standard of rest (LSR) using the velocity of the Sun taken from Dehnen & Binney (1998). We adopted a right-handed coordinate system, in which U, V, and W are positive towards the Galactic center, the Galactic rotation and the Galactic north pole, respectively. The code input parameters were taken from the Hipparcos catalogue, with the exception of the radial velocities, which were determined by us when Doppler velocity corrections were applied to the FEROS spectra. Four of our objects (HD 22 484, HD 22 879, HD 76 932, and HD 182 572) have radial velocities determined with the CORAVEL spectrometers (Udry et al. 1999), which have high precision and accuracy, and there is excellent agreement between these and our results (linear correlation with dispersion $\sigma = 0.05 \text{ km s}^{-1}$). Mark that HD 182 572, although initially selected, was not included in the final sample, because we could not obtain Th spectra for this object; nonetheless, we used it for comparison with Udry et al. (1999) because we had its FEROS spectrum and its derived radial velocity (-100.8 km s^{-1}). Distances were calculated directly from the trigonometric parallaxes; extinction was not corrected for, as it can be considered negligible due to the proximity of our objects (less than 40 pc). Our results are contained in Table 2, along with the radial velocities used in the calculations.

It is not possible to discriminate the disk from the halo population based on kinematic or metallicity criteria, independently. Nonetheless, this discrimination can be achieved using these criteria *simultaneously*. Schuster et al. (1993) demonstrated that halo stars whose metallicities are higher than $[\text{Fe}/\text{H}] = -1.00$ have V velocity component lower than disk

Table 2. Radial velocities (RV) and spatial velocity components (U, V, and W) of the sample stars, in a right-handed Galactic system and relative to the LSR. All values are in km s^{-1} .

HD	RV	U	V	W
2151	+23.7	-50.4 \pm 1.2	-41.9 \pm 0.9	-24.5 \pm 0.4
9562	-14.0	+1.4 \pm 0.5	-21.2 \pm 0.8	+20.2 \pm 0.4
16 417	+11.8	+32.1 \pm 0.5	-18.4 \pm 0.7	-2.0 \pm 0.4
20 766	+12.8	-60.5 \pm 0.9	-42.1 \pm 0.9	+22.8 \pm 0.6
20 807	+12.1	-60.0 \pm 0.8	-41.3 \pm 0.9	+23.2 \pm 0.6
22 484	+28.1	+11.2 \pm 0.4	-10.0 \pm 0.6	-34.8 \pm 0.5
22 879	+120.7	-99.7 \pm 0.6	-80.5 \pm 1.6	-37.7 \pm 0.9
30 562	+77.3	-42.1 \pm 0.5	-67.5 \pm 1.3	-13.9 \pm 0.6
43 947	+41.6	-29.8 \pm 2.0	-6.1 \pm 0.8	+4.6 \pm 0.4
52 298	+4.0	+70.9 \pm 1.2	+1.4 \pm 0.6	-15.2 \pm 0.6
59 984	+55.4	+9.1 \pm 0.8	-74.8 \pm 1.0	-21.8 \pm 0.8
63 077	+106.2	-137.1 \pm 1.0	-55.6 \pm 0.8	+45.9 \pm 0.5
76 932	+119.7	-38.1 \pm 0.4	-84.9 \pm 0.7	+76.7 \pm 0.8
102 365	+17.4	-49.7 \pm 0.7	-33.7 \pm 0.7	+12.5 \pm 0.4
128 620	-23.9	-21.1 \pm 0.7	+7.3 \pm 0.9	+19.8 \pm 0.4
131 117	-28.6	-50.2 \pm 1.5	-29.6 \pm 1.8	+17.4 \pm 1.0
160 691	-8.9	-3.6 \pm 0.4	-3.2 \pm 0.6	+3.2 \pm 0.4
196 378	-31.5	-55.2 \pm 1.2	-42.6 \pm 1.2	+5.9 \pm 1.0
199 288	-7.4	+32.7 \pm 0.8	-96.4 \pm 1.9	+51.8 \pm 1.0
203 608	-29.4	-2.7 \pm 0.4	+48.9 \pm 0.6	+12.6 \pm 0.4

stars of the same metallicity, and that it is possible to separate these populations with a line in the V vs. $[\text{Fe}/\text{H}]$ diagram. Analyzing such diagram constructed for our sample

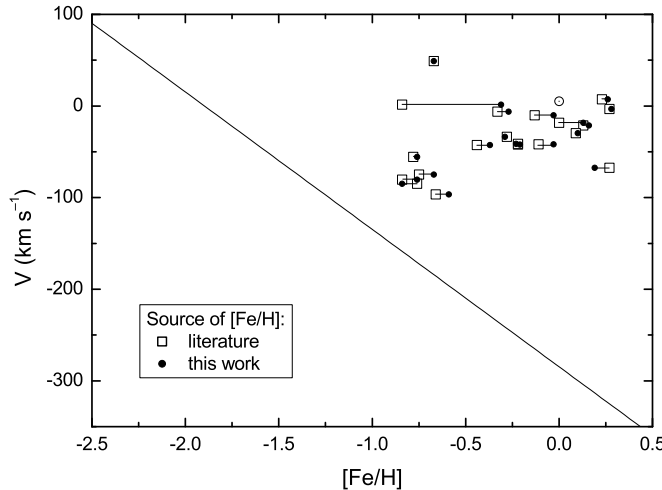


Fig. 1. V vs. $[\text{Fe}/\text{H}]$ diagram for the sample stars. The diagonal line is a cut off between the halo and the disk populations (below and above, respectively). Velocity components V were calculated by us. The metallicities initially employed, represented as open squares, were taken from the literature (Table 4); small filled circles represent metallicities derived in this work.

stars (Fig. 1), we can see that all of them are located far above the cut off line, indicating a highly remote probability of one of them belonging to the halo. Note that the metallicities used for the graph were taken from papers individually chosen among the spectroscopic determinations that compose the Cayrel de Strobel et al. (2001) catalogue, i.e., they were not determined by us. Even though they could have been wrong, these determinations would have to have been *overestimated* by at least 0.52 dex for a star to cross the line, which is very unlikely. After having determined our own metallicities (Table 7), we confirmed that results from the literature are overestimated by 0.08 dex at most, when compared to our results.

According to Buser et al. (1998), the local density of thin disk, thick disk, and halo stars in the Galaxy conforms to the proportion 2000:108:1, respectively. If we take a completely random sample of 20 stars, there is a 34.9 % probability that it will be totally free of thick disk stars. The probability that it will contain 3 or more thick disk stars is low (8.0 %). Consequently, if there are thick disk stars in our sample, they can be regarded as a contamination without significant bearing on our results.

2.3. ESO 1.52 m telescope spectra

Observations with the ESO 1.52 m telescope were performed by the authors in two runs, in March and August, 2001. All obtained FEROS spectra have high nominal resolving power ($R = 48\,000$), signal-to-noise ratio ($\text{S/N} \geq 300$ in the visible) and coverage (3500 Å to 9200 Å spread over 39 échelle orders). Spectra were acquired for all sample stars and for the Sun (Ganymede), and were used for atmospheric parameter and chemical abundance determination. Order #9 of the FEROS spectra, which extends from 4039 Å to 4192 Å, was used for the determination of Eu abundances by synthesis of the Eu II line at 4129.72 Å.

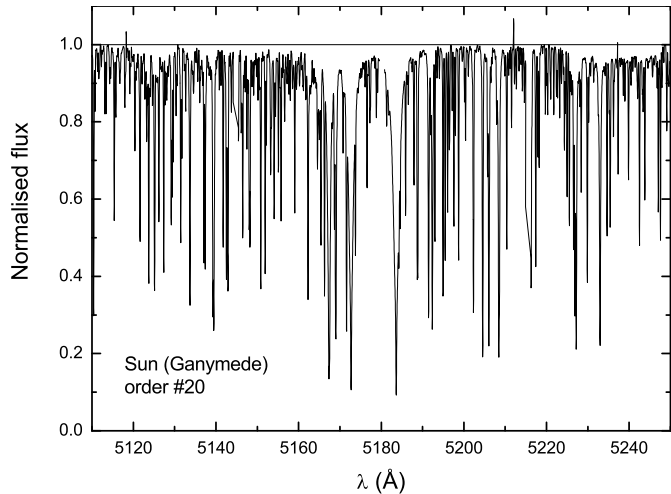


Fig. 2. Example of a solar (Ganymede) normalised FEROS spectrum (order #20), obtained with the ESO 1.52 m telescope.

FEROS spectra are reduced automatically by a MIDAS script during observation, immediately after the CCD read out. Reduction is carried out in the conventional way, applying the following steps: bias, scattered light, and flat field corrections, extraction, wavelength calibration (using ThAr calibration spectra), and baricentric radial velocity correction. As a last step, the reduction script merges all échelle orders to form one continuous spectrum with a 5200 Å coverage. However, the merge process is sometimes faulty, and strong curvatures and discontinuities are introduced in the final spectrum as result. It becomes difficult to distinguish between the “natural” curvature of the spectrum and that introduced by the merge, and the continuum normalization procedure is rendered very insecure. We chose to re-reduce all spectra, employing the same script used for the automatic reduction, but eliminating the merge, so that we could work with each order independently. Unfortunately, after the re-reduction we found out that each individual order is plagued by a strong discontinuity itself, which demonstrates that some reduction steps prior to the merge are also faulty. We corrected this by simply trimming each order and retaining only the section beyond the discontinuity. As there are intersections in wavelength coverage between adjacent orders, total loss of coverage caused by the trimmings was only ~ 500 Å. After trimming the orders, we corrected them for the stellar radial velocity. Stars that were observed more than once had their spectra averaged, using their S/N ratio as weight. Finally, the spectra were normalised by fitting selected continuum windows with order 2 to 5 Legendre polynomials. Figure 2 is an example of a solar (Ganymede) normalised ESO spectrum.

2.4. OPD spectra

Observations at OPD were performed by the authors in five runs, in May and October, 2000, and in May, August and October, 2002. The instrumental set-up was the following: 1800 lines mm^{-1} grating, 250 µm slit, 1024 24µm-pixel back-illuminated CCD (#101 or #106). All obtained spectra have

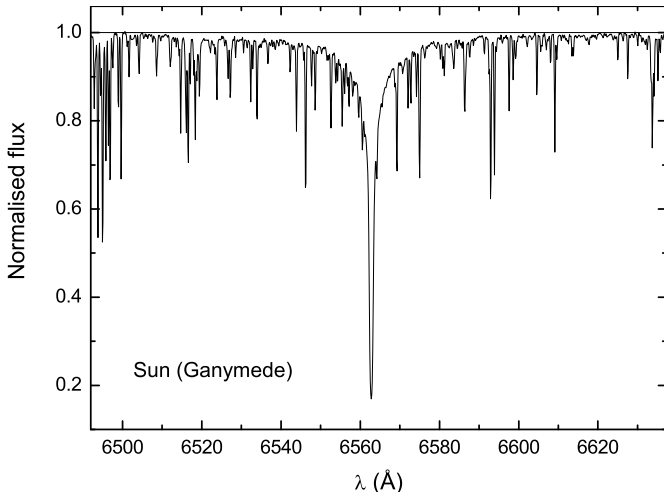


Fig. 3. Example of a solar (Ganymede) normalised OPD spectrum.

moderate nominal resolving power ($R \sim 22\,000$) and high signal-to-noise ratio ($S/N \geq 200$). The spectra are centered at the $H\alpha$ line (6562.8 \AA) and cover $\sim 150 \text{ \AA}$. Spectra were obtained for all sample objects, with the exception of HD 9562, and for the Sun (Ganymede), and were used for T_{eff} determination through profile fitting (Sect. 3.2.2). FEROS spectra can not be used for this purpose because the échelle order #29, which contains $H\alpha$, has an useful range of 6430 \AA to 6579 \AA , leaving only 16 \AA at the red wing of the line. Since $H\alpha$ is very broad, it does not reach continuum levels this close to its center, precluding normalisation. On the hand, OPD spectra reach 75 \AA at each side of $H\alpha$, allowing the selection of reliable continuum windows.

Reduction was performed using IRAF, following the usual steps of bias, scattered light and flat field corrections, and extraction. Wavelength calibration was performed individually for each star by comparing the central wavelength of selected absorption lines with their laboratory values. This way, Doppler corrections were not necessary, since the wavelength calibration corrects the spectra to the rest frame. Finally, spectra were averaged and normalised in the same way the ESO spectra were. Figure 3 is an example of a solar (Ganymede) normalised OPD spectrum.

2.5. ESO 3.60 m telescope and CAT spectra

Observational spectra for the Th abundance determinations were obtained with the CES fed by the ESO 3.60 m telescope, for 16 of the 20 sample stars and for the Sun. Observations were carried out by the authors in January, 2002. Spectra were obtained with the blue optical path and the high resolution image slicer (nominal resolving power $R \sim 235\,000$). However, unknown problems during the observations degraded the effective resolving power down to $R \sim 130\,000$. The spectra were centered at the Th II line (4019.13 \AA) and have a 27 \AA coverage. Due to the low efficiency of the spectrograph at 4000 \AA , we limited the signal-to-noise ratio to $S/N \sim 200$ for stars with visual magnitude $V \geq 6$ and $S/N \sim 300$ for brighter objects.

Table 3. Available observations.

HD	FEROS	OPD	CES + 3.60 m	CES + CAT	
				Europium	Thorium
2151	✓	✓	✓	✓	✓
9562	✓		✓		
16417	✓	✓	✓		
20766	✓	✓	✓		✓
20807	✓	✓	✓	✓	✓
22484	✓	✓	✓	✓	✓
22879	✓	✓	✓		
30562	✓	✓	✓		
43947	✓	✓	✓		
52298	✓	✓	✓		
59984	✓	✓	✓		
63077	✓	✓	✓		✓
76932	✓	✓	✓		
102365	✓	✓	✓		
128620	✓	✓	✓	✓	✓
131117	✓	✓	✓		
160691	✓	✓		✓	✓
196378	✓	✓		✓	✓
199288	✓	✓			✓
203608	✓	✓		✓	✓

CES spectra were also obtained with the ESO's CAT, with the aim of determining the abundances of both Eu and Th. Observations were carried out by the authors in August, 1998. Not all sample objects have been observed: we obtained Eu spectra for 8 stars and the Sun, and Th spectra for 9 stars and the Sun. All spectra have high resolving power ($R = 100\,000$ for Th, and $R = 50\,000$ for Eu), and high signal-to-noise ratio ($S/N \sim 300$); coverage is 18 \AA . Table 3 details which objects were observed with which instruments and telescopes.

Reduction followed the usual steps of bias and flat field corrections, extraction and wavelength calibration (using ThAr calibration spectra). Correction for the stellar radial velocities was implemented by comparing the wavelengths of a number of absorption lines with their rest frame wavelengths. Finally, the spectra were normalised by fitting selected continuum windows with order 2 to 5 Legendre polynomials. Stars that were observed in more than one night did *not* have spectra from different nights averaged. Figure 4 shows as an example a solar (sky) normalised CES spectrum, observed with the 3.60 m. Examples of solar (sky) normalised CES spectra, observed with the CAT, are presented in Fig. 5 (for the Eu region), and in Fig. 6 (for the Th region).

3. Atmospheric parameters

Atmospheric parameters (effective temperatures, surface gravities, microturbulence velocities (ξ), and metallicities) have been obtained through an iterative and totally self-consistent procedure, composed of the following steps:

1. Determine photometric T_{eff} ([Fe/H] from literature).
2. Determine $\log g$.
3. Determine T_{eff} from $H\alpha$ fitting.
4. Set $T_{\text{eff}} = (\text{photometric} + H\alpha)/2$.

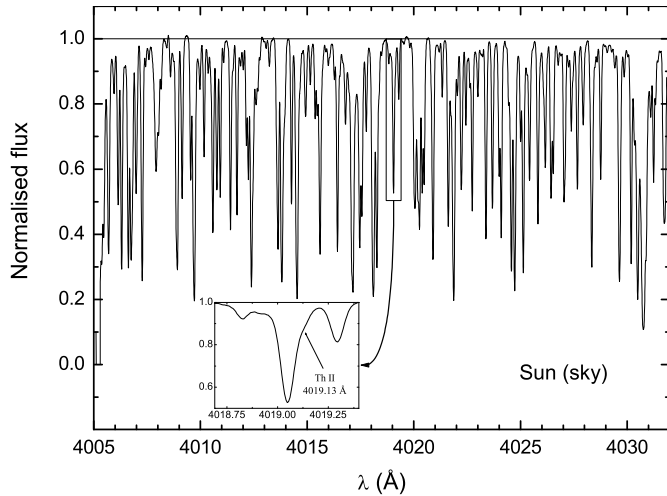


Fig. 4. Example of a solar (sky) normalised CES spectrum, observed with the ESO 3.60 m telescope, in the Th II line region at 4019.13 Å. The inset shows the Th II line in greater detail.

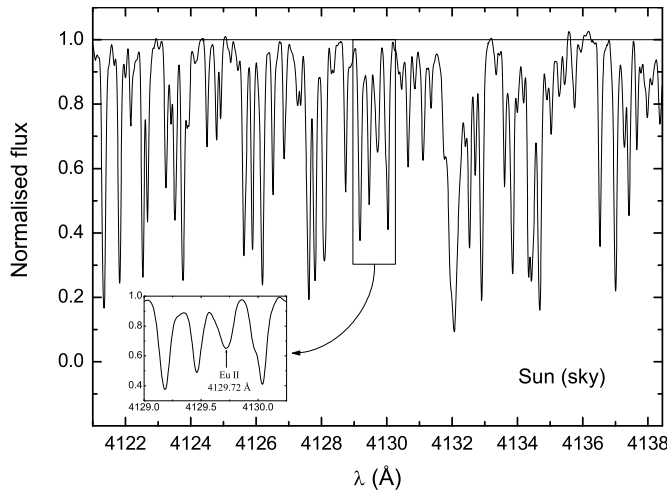


Fig. 5. Example of a solar (sky) normalised CES spectrum, observed with the ESO CAT, in the Eu II line region at 4129.72 Å. The inset shows the Eu II line in greater detail.

5. Determine [Fe/H] and ξ .
6. Determine photometric T_{eff} ([Fe/H] from step 5).
7. Set $T_{\text{eff}} = (\text{photometric} + H\alpha)/2$.
8. Have the parameters changed since step 8 of last iteration?
If yes, go back to step 2.
9. END.

Notice that a minimum of 2 iterations is required, since in step 8 we must compare the results obtained with those from the preceding iteration. Input parameters for each step are simply the output parameters of the preceding step. At all times, the adopted effective temperature is the average of the two determinations (photometric and from $H\alpha$ fitting). Owing to this, a new average is performed each time a new determination is made (steps 4 and 7, following T_{eff} determinations by $H\alpha$ fitting and photometry, respectively). The techniques used at each step are described in the next sections, and the final results are presented in Table 7.

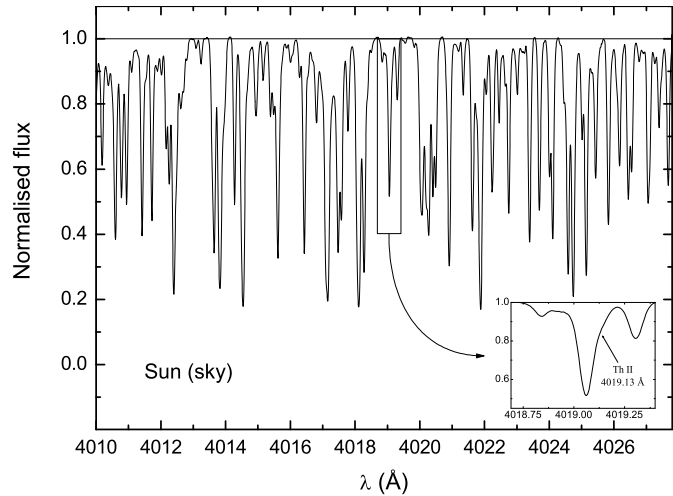


Fig. 6. Example of a solar (sky) normalised CES spectrum, observed with the ESO CAT, in the Th II line region at 4019.13 Å. The inset shows the Th II line in greater detail.

3.1. Model atmospheres and partition functions

The determination of effective temperatures through $H\alpha$ profile fitting, and of microturbulence velocities and chemical abundances through detailed spectroscopic analysis, demands the use of model atmospheres. Those employed by us were the plane parallel, flux constant, LTE model atmospheres described and discussed in detail by Edvardsson et al. (1993). The $T(\tau)$ laws were interpolated using a code gently made available by Monique Spite (Observatoire de Paris-Meudon, France). Throughout this work, we have used [Fe/H] as the metallicity of the model atmosphere. Partition functions were calculated by us using the polynomial approximations of Irwin (1981).

3.2. Effective temperature

3.2.1. Photometric calibrations

We determined effective temperatures using the photometric calibrations from Porto de Mello et al. (2005). These metallicity-dependent calibrations were constructed using highly accurate effective temperatures obtained with the infrared flux method (Blackwell et al. 1980, 1991), and make use of the ($B - V$) and ($V - K$) Johnson, ($b - y$) and β Strömgren, and ($B_T - V_T$) Hipparcos colour indices:

$$\begin{aligned}
 T_{\text{eff}}(K) &= 7747 - 3016(B - V)\{1 - 0.15[\text{Fe/H}]\}, \quad \sigma = 65 \text{ K} \\
 T_{\text{eff}}(K) &= 8974 - 2880(V - K) + 440(V - K)^2, \quad \sigma = 50 \text{ K} \\
 T_{\text{eff}}(K) &= 8481 - 6516(b - y)\{1 - 0.09[\text{Fe/H}]\}, \quad \sigma = 55 \text{ K} \\
 T_{\text{eff}}(K) &= \sqrt{\beta - 2.349}, \quad \sigma = 70 \text{ K} \\
 T_{\text{eff}}(K) &= 7551 - 2406(B_T - V_T)\{1 - 0.2[\text{Fe/H}]\}, \quad \sigma = 64 \text{ K}
 \end{aligned}$$

A complete description of the derivation of these calibrations is given in Porto de Mello et al. (2005).

Table 4 contains photometric data from the literature. The only sample star absent on the table is HD 128620 (α Cen A), whose photometric data is unreliable due to its high apparent magnitude. The metallicities presented in the table were taken from papers individually chosen from the

Cayrel de Strobel et al. (2001) catalogue, with the exception of HD 160 691 (Porto de Mello et al. 2005), and were only used on step 1 of the atmospheric parameter determination for each star. The $(b - y)$ colour indices taken from Grønbech & Olsen (1976, 1977) and Crawford et al. (1970) were originally in the Olsen (1983) photometric system. Since the calibration used by us was based on the Olsen (1993) photometric system, we converted the afore-mentioned data to this system through the relation $(b - y)_{\text{Olsen 1993}} = 0.8858 (b - y)_{\text{Olsen 1983}} + 0.0532$, which is Equation (1) from Olsen (1993).

Photometric temperatures have been averaged using the maximum likelihood method, assuming that each value follows a gaussian probability distribution, which results in

$$\overline{T_{\text{eff}}} = \sum_{i=1}^N \frac{T_{\text{eff}} i}{\sigma_i^2} \left/ \sum_{i=1}^N \frac{1}{\sigma_i^2} \right.,$$

where N is the number of calibrations effectively used. We took the standard deviation of the averages as their uncertainties. These vary from 27 K to 37 K, and such a short range prompted us to adopt a single value $\sigma = 32$ K for the average photometric T_{eff} of each sample star. Take heed that these are internal uncertainties only; for a detailed discussion, see Porto de Mello et al. (2005). Final photometric effective temperatures are presented in Table 7.

3.2.2. $\text{H}\alpha$ profile fitting

The $\text{H}\alpha$ profiles have been studied in detail (by da Silva 1975, Gehren 1981, Fuhrmann et al. 1993, 1994, Gratton et al. 1996, and Cowley & Castelli 2002, among others), and have been shown, in the case of cool stars, to be rather insensitive to surface gravity, microturbulence velocity, metallicity, and mixing length parameter variations. They are, notwithstanding, very sensitive to the effective temperature of the atmosphere. By comparing the observations with theoretical profiles calculated for various effective temperatures, we can estimate this atmospheric parameter.

Theoretical profiles were calculated with a code developed by us from the original routines of Praderie (1967). This code takes into account the convolution of radiative, Stark (Vidal et al. 1971), Doppler and self-resonance (Cayrel & Traving 1960) broadenings.

In order to check the accuracy of the determinations, we analysed the solar spectrum (Fig. 7). The adopted solar parameters were $T_{\text{eff}} = 5777$ K (Neckel 1986), $\log g = 4.44$, $[\text{Fe}/\text{H}] = 0.00$, microturbulence velocity $\xi = 1.15$ km s $^{-1}$ (Edvardsson et al. 1993), and $n(\text{He})/n(\text{H}) = 0.10$. The obtained temperature was 5767 K, 10 K lower than the solar value adopted by us. This small discrepancy was corrected by adding +10 K to all stellar effective temperatures determined by $\text{H}\alpha$ profile fitting.

Uncertainties in the determinations were estimated using the Sun as a standard (Table 5). The influence of atmospheric parameter uncertainties were evaluated changing these parameters (one at a time) by an amount deemed representative of their uncertainties, and then redetermining the effective temperature. We tested the influence of the continuum placement

Table 5. Uncertainty of the effective temperatures determined by $\text{H}\alpha$ profile fitting, using the Sun as a standard. For detailed explanation, see text.

Parameter	Parameter uncertainty	T_{eff} uncertainty
Continuum	0.20 %	25 K
$\log g$	0.20 dex	20 K
$[\text{Fe}/\text{H}]$	0.08 dex	5 K
ξ	0.10 km s $^{-1}$	5 K
Personal judgement	–	20 K
Blue/red wings	–	20 K
TOTAL	–	43 K

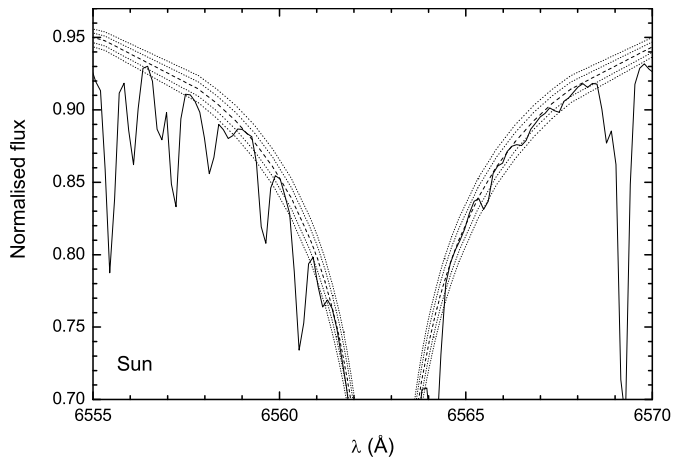


Fig. 7. $\text{H}\alpha$ profile of the Sun. Dashed line is the best fit (5767 K). Dotted lines show profiles computed when the effective temperature was changed by ± 50 K and ± 100 K.

uncertainty, which is $\sim 0.2\%$, by multiplying the flux by 1.002, and redetermining the temperature. Since the fitting of theoretical profile to the observation is done via a *fit-by-eye* technique, the personal judgement of who is making the analysis introduces uncertainty to the obtained temperature; we estimated this uncertainty to be ~ 20 K. Finally, some uncertainty comes from the difference between blue and red wings, which are best fit by profiles of effective temperatures differing by ~ 20 K. The total uncertainty was estimated at 43 K by the root-mean-square (RMS) of the individual sources cited above. Final $\text{H}\alpha$ effective temperatures are presented in Table 7.

3.2.3. Adopted effective temperatures

The adopted effective temperature for each star was the arithmetic mean of the photometric and $\text{H}\alpha$ determinations, after convergence was achieved in the iterative procedure. The uncertainty of the adopted T_{eff} was taken as the standard deviation of the mean, resulting in 27 K.

Table 4. Photometric indices and metallicities for all sample stars. Metallicities were taken from the literature for use in the kinematic characterization of the sample (Sect. 2.2) and as input for the first step in the iterative determination of atmospheric parameters (Sect. 3.2).

HD	(B-V)	Ref.	(b-y)	Ref.	(V-K)	Ref.	β	Ref.	(B _T -V _T)	Ref.	[Fe/H]	Ref.
2151	0.62	1	0.379	3	—	—	2.597	11	—	—	-0.11	15
9562	0.64	1	0.408	3	1.422	13	2.585	10	0.709	14	+0.13	16
16 417	0.66	1	0.412	3	—	—	—	—	0.730	14	+0.00	17
20 766	0.64	1	0.404	4	1.537	13	2.586	5	—	—	-0.22	18
20 807	0.60	1	0.383	4	—	—	2.592	5	—	—	-0.22	18
22 484	0.58	1	0.363	3	1.363	13	2.608	5	0.626	14	-0.13	19
22 879	0.54	2	0.369	3	—	—	—	—	0.581	14	-0.84	20
30 562	0.62	1	0.403	3	1.410	13	2.610	5	0.709	14	+0.27	21
43 947	—	—	0.377	6	—	—	2.598	6	0.604	14	-0.33	19
52 298	0.46	2	0.320	3	—	—	—	—	0.500	14	-0.84	22
59 984	0.54	1	0.354	7	—	—	2.599	5	0.566	14	-0.75	23
63 077	0.60	1	0.387	5	—	—	2.590	5	—	—	-0.78	23
76 932	0.53	1	0.368	5	1.410	13	2.595	5	0.556	14	-0.76	16
102 365	0.66	1	0.411	3	—	—	2.588	6	—	—	-0.28	24
131 117	0.60	1	0.389	4	—	—	2.621	9	0.662	14	+0.09	16
160 691	0.70	1	0.433	3	—	—	—	—	0.786	14	+0.27	24
196 378	0.53	1	0.369	5	—	—	2.609	5	0.579	14	-0.44	23
199 288	0.59	2	0.393	6	—	—	2.588	6	0.638	14	-0.66	25
203 608	0.49	1	0.338	8	1.310	12	2.611	8	0.522	14	-0.67	23

References: 1 - Warren & Hoffleit (1987); 2 - Mermilliod (1987); 3 - Olsen (1994); 4 - Olsen (1993); 5 - Grönbech & Olsen (1976, 1977); 6 - Olsen (1983); 7 - Manfroid & Sterken (1987); 8 - Crawford et al. (1970); 9 - Olsen & Perry (1984); 10 - Crawford et al. (1966); 11 - Hauck & Mermilliod (1998); 12 - Koornneef (1983); 13 - di Benedetto (1998); 14 - Perryman & ESA (1997); 15 - Castro et al. (1999); 16 - Gratton et al. (1996); 17 - Gehren (1981); 18 - del Peloso et al. (2000); 19 - Chen et al. (2000); 20 - Fuhrmann (1998); 21 - da Silva & Porto de Mello (2000); 22 - Hartmann & Gehren (1988); 23 - Edvardsson et al. (1993); 24 - Porto de Mello et al. (2005); 25 - Axer et al. (1994).

3.3. Surface gravity

Surface gravities were estimated from effective temperatures, stellar masses and luminosities, employing the known equation

$$\log\left(\frac{g}{g_\odot}\right) = \log\left(\frac{m}{m_\odot}\right) + 4 \log\left(\frac{T_{\text{eff}}}{T_{\text{eff}\odot}}\right) + 0.4 (M_{\text{bol}} - M_{\text{bol}\odot}), \quad (1)$$

in which we adopted $M_{\text{bol}\odot} = 4.75$ (Neckel 1986).

Luminosities were calculated by us from the visual magnitudes of Table 1 and bolometric corrections from Habets & Heintze (1981). Stellar masses were estimated using HR diagrams with the Gen92/96 sets of evolutionary tracks. Each diagram was calculated by Gen92/96 for 1 of 5 different metallicities ($Z = 0.0010, 0.0040, 0.0080, 0.0200$, and 0.0400 , with $Z_\odot = 0.0188$), with tracks for 5 different masses ($0.80, 0.90, 1.00, 1.25$, and $1.50 m_\odot$). Masses were estimated for each star, interpolating among the tracks calculated for the metallicities above. Then, we interpolated among metallicities to obtain the correct mass for the star. Figure 8 presents one such diagram, calculated for $Z = 0.0200$, in which we used the final, adopted effective temperatures and metallicities (Table 7).

In order to check the accuracy of the determinations, we estimated the solar mass itself in the Gen92/96 diagrams. The obtained value was $0.97 m_\odot$. This discrepancy was corrected by adding $+0.03 m_\odot$ to surface gravities obtained for the sample stars.

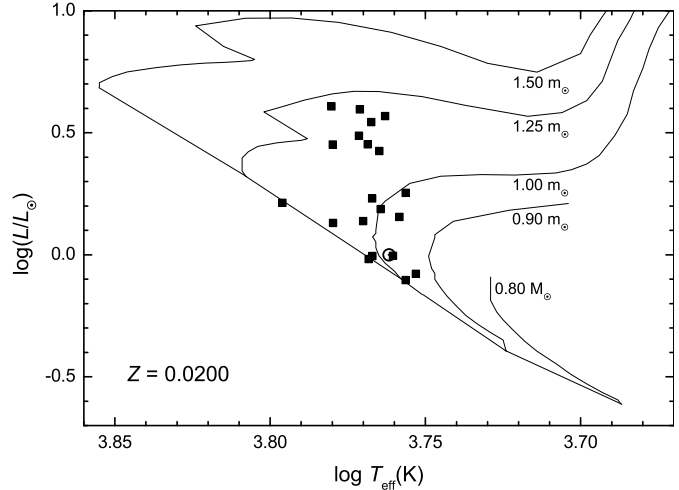


Fig. 8. Example of a Gen92/96 set of evolutionary tracks, for $Z = 0.0200$. Filled squares are the sample stars, after convergence of the atmospheric parameter determination procedure. The Sun is represented by the symbol \odot . The effective temperatures and metallicities are the final, adopted values (Table 7).

The uncertainty of the surface gravities was obtained by error propagation from Equation (1), resulting in the expression

$$\sigma_{\log g} = \sqrt{\sigma_{\log(m/m_\odot)}^2 + 16 \sigma_{\log T_{\text{eff}}}^2};$$

analysis showed that the influence of the bolometric magnitude uncertainty is negligible, and as such it was not taken into consideration.

Stellar mass uncertainty is a function of the position of the star in the HR diagram. Stars located in regions where the evolutionary tracks are closer together will have larger errors than those located between tracks further apart. Nevertheless, we have chosen to adopt a single average uncertainty of $0.03 m_{\odot}$, so as to simplify the calculations. Taking stellar masses and effective temperatures typical of our sample ($1.00 m_{\odot}$ and 6000 K, respectively), we have $\sigma_{\log T_{\text{eff}}} = 1.9 10^{-3}$ and $\sigma_{\log(m/m_{\odot})} = 1.3 10^{-2}$, and consequently $\sigma_{\log g} = 0.02$ dex. This value does not take into consideration the uncertainties intrinsic to the calculation of evolutionary tracks, which are very difficult to assess.

3.4. Microturbulence velocity and metallicity

Microturbulence velocities and metallicities have been determined through detailed, differential spectroscopic analysis, relative to the Sun, using EWs of Fe I and Fe II lines. In such differential analysis, the Sun is treated like any other sample star: its spectra are obtained under the same conditions, with the same resolving power, signal-to-noise ratio, and equipment, and are reduced by the same procedures; the same model atmospheres and analysis codes are utilised. This way, systematic errors and eventual non-LTE effects are reduced, because they are partially cancelled out.

3.4.1. Equivalent width measurements

We were not interested solely in Fe lines, but also in the lines of other elements that contaminate the spectral regions of the Th II line in 4019.13 Å (V, Cr, Mn, Co, Ni, Ce, and Nd), and of the Eu II line in 4129.72 Å (Ti, V, Cr, Co, Ce, Nd, and Sm), whose EWs were then used for the abundance determinations of Sect. 4.

An initial list of lines was constructed from Moore et al. (1966), Steffen (1985), Cayrel de Strobel & Bentolila (1989), Brown & Wallerstein (1992), Furenlid & Meylan (1990), and Meylan et al. (1993). Then, a series of selection criteria were applied: lines with wavelengths lower than 4000 Å were removed, since the line density in this region is very high, lowering the continuum and rendering its normalization insecure, besides making it too difficult to find acceptably isolated lines; lines with wavelengths greater than 7000 Å were discarded, due to excessive telluric line contamination in this region; lines with $\text{EW} > 110 \text{ m}\text{\AA}$ in the Sun, which are more sensitive to uncertainties in microturbulence velocity due to saturation, were eliminated; only isolated lines were kept, eliminating those with known contaminations; lines whose EWs could not have been, for any reason, accurately measured in the solar spectra, were rejected.

EWs have been measured by gaussian profile fitting. In order to check the measurement accuracy, we compared our solar EWs with those from Meylan et al. (1993). The EWs from Meylan et al. were measured by Voigt profile fitting, using the

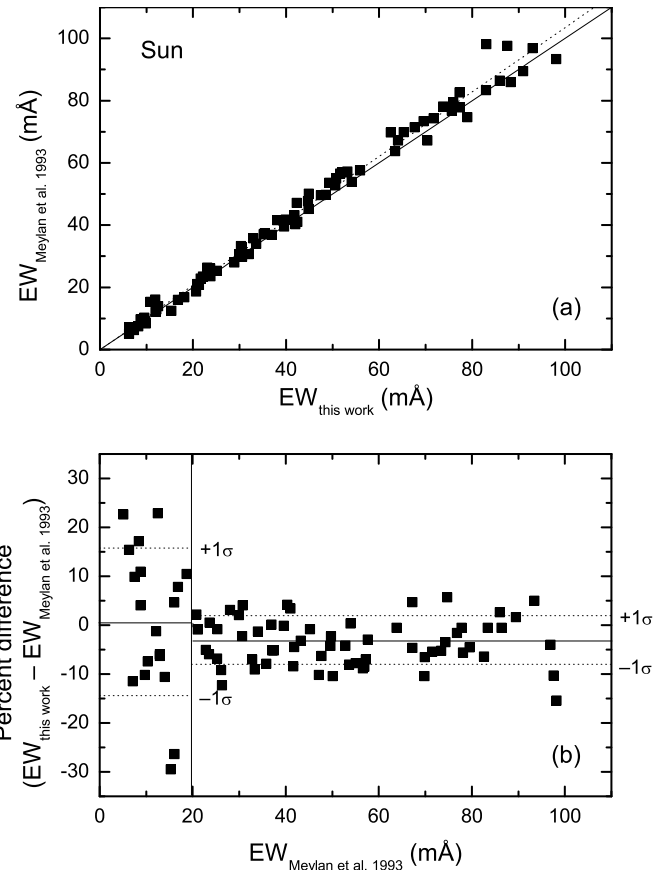


Fig. 9. Panel (a): Comparison between our solar EWs and those from Meylan et al. (1993). Solid line corresponds to a $y = x$ relation, and the dotted one is a linear regression. Panel (b): Percent differences between the same EWs. Solid lines correspond to mean differences, and the dotted ones represent the mean differences modified by their standard deviations ($\pm 1\sigma$).

Kurucz et al. (1984) solar atlas, which has very high resolving power and signal-to-noise ratio ($R = 522\,000$ and $S/N = 3000$, between 4500 Å and 6450 Å). A linear fit between the two data sets,

$$\text{EW}_{\text{Meylan et al. 1993}} = (1.03463 \pm 0.00649) \text{EW}_{\text{this work}},$$

shown in panel (a) of Fig. 9, presents low dispersion ($\sigma = 2.9 \text{ m}\text{\AA}$) and high correlation coefficient ($R = 0.994$). This relation is used to correct all our EWs. The mean percent difference between the measurements is -2.5% , presenting no dependence on the EW (Fig. 9, panel (b)). The larger percent differences exhibited by the weakest lines are expected, since these are more prone to uncertainties. More than 86% of the lines agree at a 10% level.

A last selection criterium was applied to the line list: given the $2.9 \text{ m}\text{\AA}$ dispersion of the linear relation between our EWs and those from Meylan et al., we rejected all Fe lines with $\text{EW} < 6 \text{ m}\text{\AA}$ (i.e., $\sim 2\sigma$). This criterium was not implemented for the lines of the other elements because they have fewer interesting lines available, and a cut off at $6 \text{ m}\text{\AA}$ would be too restrictive. The final list of lines is composed of 65 Fe I, 10 Fe II, 31 Ti, 6 V, 21 Cr, 6 Mn, 8 Co, 13 Ni, 5 Ce, 2 Nd, and 1 Sm lines,

Table 6. A sample of the EW data. The complete content of this table is only available in electronic form at the CDS. For a description of the columns, see text (Sect. 3.4.1).

λ (Å)	Element	χ (eV)	$\log gf$	Sun	...	HD 203 608
5657.436	V I	1.06	-0.883	9.5	...	0.0
5668.362	V I	1.08	-0.920	8.5	...	0.0
5670.851	V I	1.08	-0.452	21.6	...	0.0
⋮	⋮	⋮	⋮	⋮	⋮	⋮
5427.826	Fe II	6.72	-1.371	6.4	...	0.0
6149.249	Fe II	3.89	-2.711	40.9	...	24.7

in the Sun. Not all these lines have been used for all sample stars, since random events, like excessive profile deformation by noise, prevented sometimes an accurate measurement.

Table 6 presents a sample of the EW data. Its complete content, composed of the EWs of all measured lines, for the Sun and all sample stars, is only available in electronic form at the CDS.³ Column 1 lists the central wavelength (in angstroms), Column 2 gives the element symbol and degree of ionization, Column 3 gives the excitation potential of the lower level of the electronic transition (in eV), Column 4 presents the solar $\log gf$ derived by us, and the subsequent Columns present the EWs, in mÅ, for the Sun and the other stars, from HD 2151 till HD 203 608 (in order of increasing HD number).

3.4.2. Spectroscopic analysis

The first step of the spectroscopic analysis consisted of determining *solar* $\log gf$ values for all measured lines. For such determination, we employed a code written by us, based on routines originally developed by Monique Spite. This code calculates the $\log gf$ that an absorption line must have for its abundance to be equal to the standard solar value from Grevesse & Sauval (1998), given the solar EW and lower excitation potential of the line. For all stars, chemical abundances were determined using these solar $\log gf$ values.

Microturbulence velocity and metallicity have been determined through a procedure which is iterative, and which can be summarised by the following sequence of steps:

1. Determine [Fe/H] for all lines, using

$$[\text{Fe}/\text{H}]_{\text{model atmosphere}} = [\text{Fe}/\text{H}]_{\text{literature}}$$
2. Set $[\text{Fe}/\text{H}]_{\text{model atmosphere}} = \text{average } [\text{Fe}/\text{H}] \text{ from lines}$.
3. Determine [Fe/H] for all lines.
4. Is $[\text{Fe}/\text{H}]_{\text{model atmosphere}} = \text{average } [\text{Fe}/\text{H}] \text{ from lines}$?
If no, go back to step 2.
5. Draw a [Fe/H] vs. EW graph for all lines, and fit a line.
6. Is the angular coefficient of the line negligible?
If no, modify ξ and go back to step 3.
7. END.

In steps 1 and 3, iron abundances are calculated line-by-line using a code very similar to the one used for the determination of the solar $\log gf$ values. The only difference is that,

³ Via anonymous ftp to cdsarc.u-strasbg.fr or via <http://cdsweb.u-strasbg.fr/cgi-bin/qcat?>

in this case, the $\log gf$ are fixed at their solar values, and an abundance is calculated for each line. In step 6, the angular coefficient is considered negligible when it is less than 25% of its own uncertainty (obtained by the fitting calculation). It is important to note that effective temperature and surface gravity remain constant at all times. In practice, the procedure is executed automatically by a code, developed by da Silva (2000). This code iterates the parameters, calculating abundances and linear fits, and making the appropriate comparisons, without human interference.

Iron abundances obtained using Fe I and Fe II lines agree very well, their differences being always lower than dispersion among the lines (as can be seen in Table 8). The differences show no dependence on any atmospheric parameter. Ionization equilibrium was not enforced by the analysis procedure, but it was, nonetheless, achieved.

Microturbulence velocity uncertainties have been estimated by varying this parameter until the uncertainty of the angular coefficient of the linear fit to the [Fe/H] vs. EW graph became equal to the coefficient itself. We found out that the uncertainties are metallicity-dependent, and can be divided into three ranges:

$$\sigma_\xi = \begin{cases} 0.23 \text{ km s}^{-1}, & [\text{Fe}/\text{H}] < -0.7 \\ 0.13 \text{ km s}^{-1}, & -0.7 \leq [\text{Fe}/\text{H}] < -0.3 \\ 0.05 \text{ km s}^{-1}, & -0.3 \leq [\text{Fe}/\text{H}] \end{cases}$$

This behaviour is expected, as the dispersion between Fe lines increases for metal-poor stars. Metallicity uncertainties were estimated in the same way that uncertainties for the other elements were (Sect. 4.2), and are presented in Table 7, along with the final, adopted values of all atmospheric parameters.

4. Abundances of contaminating elements

4.1. Abundance determination

The abundance of the elements other than iron have been determined using the same code as in Sect. 3.4.2, with the adopted atmospheric parameters and the solar $\log gf$ values.

Adopted abundances have been obtained taking the arithmetic mean of the abundances from all lines of each element, irrespective of ionization state. When dispersion between lines was less than 0.10 dex, we eliminated those that deviated by more than 2σ from the mean, and when it was more than 0.10 dex, we eliminated those that deviated by more than 1σ . The number of lines kept is presented in Tables 8 and 9, along with adopted abundances, dispersions between the lines, and uncertainties, calculated according to the procedure described in Sect. 4.2.

The lines of V, Mn, and Co exhibit hyperfine structures (HFSs) strong enough that they must be taken into account, or else severe inaccuracies would be introduced. At the resolving power achieved by FEROS, line profiles remain gaussian even for elements with important HFSs, so that we can still use the EWs we measured by gaussian profile fitting. For V and Mn lines, we took the wavelengths of the HFS components from the line lists of Kurucz (2003), whereas for the Co lines, we calculated the wavelengths ourselves

Table 7. Adopted atmospheric parameters, including the photometric and $H\alpha$ effective temperatures used to obtain the adopted mean values, and the stellar masses used to obtain the surface gravities. Uncertainties of photometric, $H\alpha$, and mean effective temperatures, and of stellar masses and surface gravities, are the same for all stars: 32 K, 43 K, 27 K, 0.03 m_\odot , and 0.02 dex, respectively.

HD	T_{eff} (K)		m_\odot	$\log g$	[Fe/H]	ξ (km s $^{-1}$)
	Phot.	$H\alpha$				
2151	5909	5799	5854	1.19	3.98	-0.03 ± 0.09
9562	5794	–	5794	1.23	3.95	$+0.16 \pm 0.09$
16 417	5821	5817	5819	1.15	4.07	$+0.13 \pm 0.09$
20 766	5696	5715	5706	0.95	4.50	-0.21 ± 0.09
20 807	5866	5863	5865	0.99	4.48	-0.23 ± 0.10
22 484	5983	6063	6023	1.16	4.11	-0.03 ± 0.09
22 879	5928	5770	5849	0.73	4.34	-0.76 ± 0.12
30 562	5883	5855	5869	1.18	4.09	$+0.19 \pm 0.09$
43 947	5940	5937	5889	0.95	4.32	-0.27 ± 0.10
52 298	6305	6200	6253	1.09	4.41	-0.31 ± 0.10
59 984	5968	5848	5908	0.97	3.96	-0.67 ± 0.11
63 077	5752	5713	5733	0.77	4.15	-0.76 ± 0.11
76 932	5874	5825	5850	0.82	4.14	-0.84 ± 0.11
102 365	5705	5620	5663	0.88	4.43	-0.29 ± 0.09
128 620	–	5813	5813	1.09	4.30	$+0.26 \pm 0.09$
131 117	5994	5813	5904	1.25	3.96	$+0.10 \pm 0.09$
160 691	5736	5676	5706	1.06	4.19	$+0.28 \pm 0.09$
196 378	6014	6044	6029	1.14	3.97	-0.37 ± 0.10
199 288	5785	5734	5760	0.82	4.35	-0.59 ± 0.10
203 608	6057	5987	6022	0.86	4.31	-0.67 ± 0.11
						1.18 ± 0.23

(del Peloso et al. 2005b). These calculations were realized using Casimir's equation (Casimir 1963), and HFS laboratory data from Guthöhrlein & Keller (1990), Pickering (1996), and Pickering & Thorne (1996). The relative intensities of the components were obtained from the calculations of White & Eliason, tabulated in Condon & Shortley (1967). A modified version of the code, which takes HFS into consideration, was used for the determination of the $\log g_f$ values and abundances.

4.2. Uncertainty assessment

Chemical abundances determined using EWs are subject to three sources of uncertainty: atmospheric parameters, EWs, and model atmospheres. If these sources were independent from one another, the total uncertainty could be estimated by their RMS. However, there is no such independency, as can be clearly perceived when the iterative character of the analysis is called to mind. In this circumstance, RMS yields an estimate of the *maximum* uncertainty. Given the extreme complexity of the interdependency between the sources of uncertainty, we did not attempt to disentangle them, and used the RMS instead.

We chose four stars as standards for the assessment, with extreme effective temperatures and metallicities: HD 160 691 (cool and metal-rich), HD 22 484 (hot and metal-rich), HD 63 077 (cool and metal-poor), and HD 59 984 (hot and metal-poor). HD 203 608 is as metal-poor as, but hotter than HD 59 984, and would apparently be better suited as a standard star; yet we did not use it, because it lacks measured V and Nd

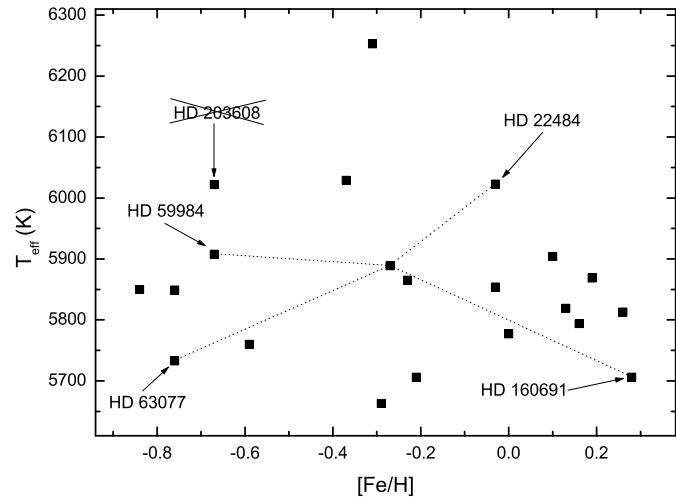


Fig. 10. Stars used as uncertainty standards are labelled. HD 203 608 was not chosen when assessing the uncertainties of contaminating elements, because it lacks V and Nd abundance determinations; however, it was chosen as the hot, metal-poor standard when assessing Eu and Th uncertainties. The effective temperatures and metallicities are the adopted ones. Dotted lines are an example of the weights used for uncertainty determination in stars not chosen as standards – see text for details.

lines, and thus could not be used to estimate the uncertainties for these elements (Fig. 10).

Initially, we determined the iron abundance uncertainty. For this purpose, we evaluated the influence of all uncertainty sources, independently. The influence of effective temperature, surface gravity and microturbulence velocity was obtained by recalculating the Fe abundances using the adopted atmospheric parameters modified, one at a time, by their own uncertainties: +27 K, +0.02 dex, and +0.05 km s $^{-1}$ (metal-rich stars) and +0.23 km s $^{-1}$ (metal-poor stars), respectively. The difference between the adopted Fe abundance and the one obtained with the modified parameter is our estimate of the influence of the parameter on the total uncertainty.

The influence of EWs was determined by recalculating the abundances using EWs modified by percentages obtained when comparing our measurements with those from Meylan et al. (1993) (Fig. 9). This comparison allows us to estimate the influence of the EW measurement per se, as well as the influence of continuum placement. The percent difference between the two sets of measurements presents a 15% dispersion for lines with $\text{EW} < 20 \text{ m}\text{\AA}$, and 5% for those with $\text{EW} > 20 \text{ m}\text{\AA}$. The Fe EWs were, then, modified by these amounts. However, this was only done for the two metal-rich standard stars. For the metal-poor stars, the influence of the continuum placement is stronger than that estimated by comparing solar EWs, because EWs are considerably lower. On the other hand, it is easier to find good continuum windows, because they are wider and more numerous. So, we compared the EWs of HD 22 879 and HD 76 932, which are metal-poor stars with very similar atmospheric parameters (specially their effective temperatures, which are virtually identical). The high similarity of atmospheric parameters mean that differences in EWs are caused almost exclusively

Table 8. Fe, Ti, V, Cr, and Mn abundances, relative to H. N is the number of absorption lines effectively used for each abundance determination, and $\sigma_{[X/H]}$ is the standard deviation of the lines of element X. The uncertainties of abundances relative to H and to Fe, calculated as described in Sect. 4.2, are also presented (as $\text{uncert.}_{[X/H]}$ and $\text{uncert.}_{[X/\text{Fe}]}$, respectively).

HD	[Fe I/H]	N	$\sigma_{[\text{Fe I/H}]}$	[Fe II/H]	N	$\sigma_{[\text{Fe II/H}]}$	[Fe/H]	N	$\sigma_{[\text{Fe/H}]}$	uncert. $_{[\text{Fe/H}]}$	[Ti/H]	N	$\sigma_{[\text{Ti/H}]}$	uncert. $_{[\text{Ti/H}]}$	uncert. $_{[\text{Ti/Fe}]}$
2151	-0.03	54	0.08	-0.03	8	0.05	-0.03	62	0.08	0.09	+0.00	29	0.12	0.09	0.02
9562	+0.16	55	0.06	+0.19	9	0.04	+0.16	64	0.06	0.09	+0.15	29	0.09	0.09	0.02
16417	+0.13	55	0.04	+0.12	8	0.03	+0.13	63	0.04	0.09	+0.14	28	0.06	0.09	0.02
20766	-0.21	51	0.05	-0.21	8	0.05	-0.21	59	0.05	0.09	-0.16	29	0.06	0.09	0.02
20807	-0.23	48	0.04	-0.25	8	0.04	-0.23	56	0.04	0.10	-0.18	28	0.07	0.09	0.02
22484	-0.03	51	0.07	-0.03	8	0.05	-0.03	59	0.07	0.09	+0.01	28	0.09	0.10	0.01
22879	-0.75	38	0.12	-0.80	8	0.08	-0.76	46	0.12	0.10	-0.46	27	0.10	0.09	0.02
30562	+0.19	58	0.05	+0.19	7	0.04	+0.19	65	0.05	0.09	+0.22	28	0.06	0.09	0.02
43947	-0.28	49	0.06	-0.22	8	0.06	-0.27	57	0.07	0.10	-0.23	27	0.10	0.09	0.02
52298	-0.31	38	0.06	-0.28	8	0.06	-0.31	46	0.06	0.10	-0.23	25	0.12	0.09	0.02
59984	-0.67	43	0.10	-0.68	8	0.11	-0.67	51	0.01	0.11	-0.48	28	0.12	0.08	0.01
63077	-0.76	43	0.12	-0.78	8	0.10	-0.76	51	0.11	0.09	-0.48	25	0.09	0.09	0.03
76932	-0.84	36	0.11	-0.84	8	0.10	-0.84	44	0.11	0.10	-0.57	27	0.08	0.09	0.02
102365	-0.28	52	0.05	-0.33	8	0.05	-0.29	60	0.05	0.09	-0.17	28	0.05	0.09	0.02
128620	+0.26	56	0.06	+0.26	9	0.04	+0.26	65	0.06	0.09	+0.29	27	0.08	0.09	0.02
131117	+0.09	53	0.05	+0.14	9	0.05	+0.10	62	0.05	0.09	+0.09	29	0.06	0.09	0.02
160691	+0.27	52	0.05	+0.33	8	0.03	+0.28	60	0.05	0.09	+0.30	29	0.07	0.09	0.02
196378	-0.37	32	0.08	-0.33	9	0.06	-0.37	41	0.07	0.10	-0.30	20	0.08	0.09	0.01
199288	-0.59	37	0.07	-0.59	8	0.06	-0.59	45	0.06	0.10	-0.38	22	0.09	0.09	0.02
203608	-0.68	36	0.10	-0.60	9	0.11	-0.67	45	0.11	0.10	-0.62	20	0.12	0.09	0.02

HD	[V/H]	N	$\sigma_{[\text{V/H}]}$	uncert. $_{[\text{V/H}]}$	uncert. $_{[\text{V/Fe}]}$	[Cr/H]	N	$\sigma_{[\text{Cr/H}]}$	uncert. $_{[\text{Cr/H}]}$	uncert. $_{[\text{Cr/Fe}]}$	[Mn/H]	N	$\sigma_{[\text{Mn/H}]}$	uncert. $_{[\text{Mn/H}]}$	uncert. $_{[\text{Mn/Fe}]}$
2151	+0.02	4	0.01	0.10	0.04	-0.04	19	0.06	0.10	0.02	-0.09	6	0.04	0.08	0.03
9562	+0.16	6	0.07	0.11	0.04	+0.18	20	0.07	0.10	0.02	+0.16	6	0.05	0.07	0.02
16417	+0.18	6	0.07	0.11	0.04	+0.14	19	0.04	0.10	0.02	+0.14	6	0.03	0.07	0.03
20766	-0.25	5	0.07	0.11	0.04	-0.21	19	0.06	0.10	0.02	-0.30	5	0.03	0.08	0.03
20807	-0.23	4	0.03	0.11	0.04	-0.23	19	0.08	0.11	0.02	-0.29	6	0.03	0.08	0.03
22484	+0.06	4	0.08	0.06	0.03	-0.03	20	0.07	0.10	0.02	-0.07	6	0.03	0.09	0.04
22879	-0.50	4	0.15	0.13	0.05	-0.69	13	0.10	0.11	0.01	-0.96	3	0.10	0.08	0.03
30562	+0.23	6	0.10	0.10	0.04	+0.20	19	0.08	0.10	0.02	+0.18	6	0.02	0.07	0.03
43947	-0.12	4	0.08	0.11	0.04	-0.27	20	0.08	0.11	0.02	-0.41	6	0.09	0.08	0.03
52298	-0.26	2	0.09	0.10	0.04	-0.30	17	0.13	0.11	0.02	-0.39	6	0.09	0.08	0.03
59984	-0.44	4	0.08	0.13	0.06	-0.67	17	0.13	0.12	0.01	-0.83	6	0.09	0.09	0.04
63077	-0.27	2	0.07	0.14	0.04	-0.67	11	0.07	0.10	0.02	-0.82	5	0.08	0.08	0.03
76932	-0.51	3	0.17	0.13	0.05	-0.76	10	0.07	0.11	0.02	-1.01	2	0.06	0.08	0.03
102365	-0.28	4	0.08	0.12	0.04	-0.28	19	0.06	0.10	0.02	-0.37	6	0.02	0.08	0.03
128620	+0.29	6	0.10	0.11	0.04	+0.26	20	0.06	0.10	0.02	+0.29	6	0.04	0.07	0.02
131117	+0.06	6	0.08	0.10	0.04	+0.11	19	0.06	0.10	0.02	+0.06	6	0.04	0.08	0.03
160691	+0.25	4	0.06	0.12	0.04	+0.28	19	0.04	0.10	0.02	+0.32	6	0.05	0.05	0.01
196378	-	0	-	-	0.04	-0.38	14	0.08	0.11	0.02	-0.44	3	0.01	0.08	0.03
199288	-0.33	3	0.02	0.13	0.04	-0.59	14	0.06	0.11	0.02	-0.77	3	0.02	0.08	0.03
203608	-	0	-	-	0.05	-0.69	9	0.09	0.11	0.01	-0.70	3	0.06	0.08	0.03

Table 9. The same as Table 8, but for Co, Ni, Ce, Nd, and Sm.

HD	[Co/H]	N	$\sigma_{[Co/H]}$	uncert. $_{[Co/H]}$	uncert. $_{[Co/Fe]}$	[Ni/H]	N	$\sigma_{[Ni/H]}$	uncert. $_{[Ni/H]}$	uncert. $_{[Ni/Fe]}$	[Ce/H]	N	$\sigma_{[Ce/H]}$	uncert. $_{[Ce/H]}$	uncert. $_{[Ce/Fe]}$
2151	+0.04	7	0.03	0.09	0.03	-0.04	11	0.05	0.11	0.02	-0.12	5	0.10	0.10	0.04
9562	+0.18	7	0.07	0.09	0.04	+0.20	11	0.09	0.10	0.02	-0.04	5	0.05	0.10	0.04
16 417	+0.16	8	0.04	0.09	0.04	+0.14	11	0.03	0.10	0.02	+0.03	5	0.06	0.10	0.04
20 766	-0.22	8	0.06	0.10	0.04	-0.22	11	0.07	0.11	0.03	-0.22	4	0.06	0.11	0.04
20 807	-0.20	8	0.06	0.09	0.04	-0.23	10	0.07	0.11	0.03	-0.31	4	0.07	0.10	0.04
22 484	-0.01	8	0.08	0.05	0.02	-0.07	9	0.05	0.10	0.01	-0.14	5	0.07	0.07	0.0
22 879	-0.55	6	0.09	0.12	0.04	-0.79	9	0.14	0.13	0.04	-0.72	5	0.05	0.13	0.05
30 562	+0.24	8	0.06	0.09	0.03	+0.23	11	0.07	0.10	0.02	+0.14	5	0.05	0.10	0.04
43 947	-0.29	8	0.06	0.09	0.04	-0.31	12	0.10	0.11	0.03	-0.29	5	0.07	0.11	0.04
52 298	-0.23	5	0.08	0.09	0.03	-0.38	5	0.05	0.11	0.03	-0.27	4	0.09	0.10	0.04
59 984	-0.54	6	0.10	0.13	0.05	-0.71	6	0.10	0.14	0.04	-0.81	5	0.04	0.14	0.05
63 077	-0.53	6	0.07	0.12	0.04	-0.62	7	0.09	0.12	0.05	-0.80	5	0.03	0.13	0.05
76 932	-0.61	4	0.02	0.11	0.04	-0.80	7	0.09	0.12	0.04	-0.81	5	0.08	0.13	0.05
102 365	-0.23	8	0.05	0.10	0.04	-0.29	10	0.05	0.11	0.03	-0.38	4	0.08	0.11	0.04
128 620	+0.30	8	0.06	0.09	0.04	+0.28	9	0.04	0.10	0.02	+0.15	5	0.08	0.10	0.04
131 117	+0.05	8	0.04	0.08	0.03	+0.12	12	0.04	0.11	0.02	-0.03	5	0.05	0.09	0.04
160 691	+0.29	8	0.04	0.09	0.04	+0.34	11	0.04	0.09	0.02	+0.18	5	0.06	0.09	0.04
196 378	-0.31	2	0.17	0.09	0.04	-0.40	8	0.11	0.12	0.03	-0.41	3	0.03	0.11	0.04
199 288	-0.39	4	0.05	0.11	0.04	-0.63	6	0.05	0.12	0.04	-0.66	3	0.07	0.12	0.05
203 608	-0.18	3	0.09	0.11	0.04	-0.74	5	0.09	0.12	0.03	-0.73	4	0.09	0.12	0.05

HD	[Nd/H]	N	uncert. $_{[Nd/H]}$	uncert. $_{[Nd/Fe]}$	[Sm/H]	N	uncert. $_{[Sm/H]}$	uncert. $_{[Sm/Fe]}$
2151	-0.03	2	0.11	0.04	-0.24	1	0.11	0.04
9562	+0.06	2	0.12	0.04	+0.06	1	0.11	0.04
16 417	+0.06	2	0.12	0.04	+0.06	1	0.11	0.04
20 766	-0.10	2	0.12	0.05	-0.11	1	0.12	0.04
20 807	-0.12	2	0.12	0.05	-0.19	1	0.11	0.04
22 484	+0.04	2	0.08	0.04	-0.13	1	0.07	0.04
22 879	-0.29	2	0.14	0.06	-0.49	1	0.13	0.05
30 562	+0.16	2	0.11	0.04	+0.14	1	0.11	0.04
43 947	-0.17	2	0.12	0.05	-0.28	1	0.11	0.04
52 298	-0.10	2	0.12	0.05	-0.29	1	0.11	0.04
59 984	-0.47	2	0.15	0.06	-0.74	1	0.14	0.05
63 077	-0.40	2	0.14	0.06	-0.85	1	0.13	0.05
76 932	-0.44	2	0.14	0.06	-0.93	1	0.13	0.05
102 365	-0.13	2	0.13	0.05	-0.23	1	0.12	0.05
128 620	+0.28	2	0.12	0.04	+0.26	1	0.11	0.04
131 117	+0.10	2	0.11	0.04	-0.11	1	0.10	0.04
160 691	+0.14	2	0.12	0.03	+0.28	1	0.12	0.04
196 378	-	0	-	-	-0.24	1	0.11	0.05
199 288	-0.32	1	0.13	0.05	-0.39	1	0.13	0.05
203 608	-	0	-	-	-0.62	1	0.12	0.05

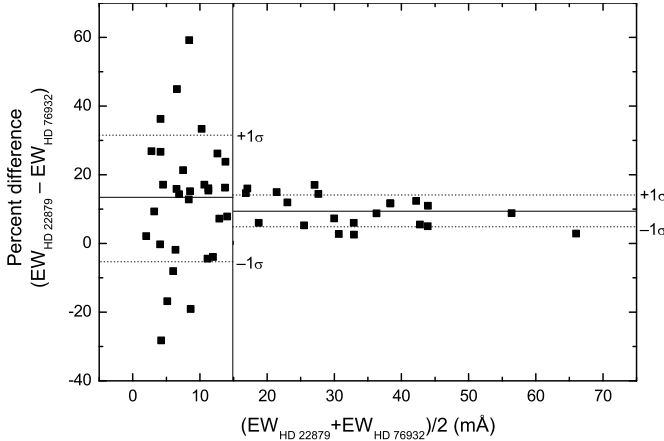


Fig. 11. Percent differences between the EWs of HD 22 879 and HD 76 932. Solid lines correspond to mean differences, and the dotted ones represent the mean differences modified by their standard deviations ($\pm 1\sigma$).

by the uncertainties in the EW measurements and continuum placement. Only Fe I lines were compared, in order to minimize the effect of the stars having slightly different surface gravities. The EW percent difference between the two stars present 19% dispersion for lines with $\text{EW} < 15 \text{ m}\text{\AA}$, and 5% for those with $\text{EW} > 15 \text{ m}\text{\AA}$ (Fig. 11); the Fe EWs of the metal-poor standard stars were modified by these values.

Log gf are also a source of uncertainty. But, since they are derived from solar EWs, their contribution is the same as that from the EWs themselves. That is to say, in practice we take into account the influence of EWs twice, so as to account for the solar EWs per se, and for the log gf values.

The influence of metallicity in the Fe abundance uncertainty is the uncertainty itself. This means that the Fe abundance uncertainty determination is, rigorously speaking, an iterative process. As a first step, Fe abundances were modified by the average dispersion *between lines* of all stars (0.07 dex). As can be seen in Table 10, the influence of metallicity is very weak. The contribution of this source would have to be 0.04 dex higher for the total uncertainty to be raised just 0.01 dex. As a second step, we should have modified the Fe abundances by the total Fe uncertainty just obtained, on the first step, by the RMS of all sources (including the metallicity itself). But, given the low contribution of this source, we stopped at the first step.

The total Fe uncertainties for the standard stars were obtained by the RMS of the six contributions: effective temperatures, surface gravities, microturbulence velocities, EWs, log gf , and metallicities. Total uncertainties for the other stars were obtained by weighted average of the standard stars values, using as weight the reciprocal of the distance of the star to each standard star, in the T_{eff} vs. [Fe/H] plane. In Fig. 10 we see an example, in which the star at the center uses the reciprocal of the lengths of the dotted lines as weights.

Uncertainties for the abundances of the other elements were determined the same way as for Fe. Although we determined individual [Fe/H] uncertainties for each star, we used a sole value of 0.10 dex when estimating the metallicity contribution to the uncertainties of the other elements. This can be justi-

fied by the low dispersion between [Fe/H] uncertainties, and by the very low sensitivity of the abundances to the metallicity of the model atmosphere. Table 10 presents contributions from the individual sources, total uncertainties, and some averages for the standard stars, relative to H. Values relative to Fe can be obtained simply by subtracting the [Fe/H] value from the [element/H] value (e.g., $\text{uncert.}_{[\text{V}/\text{Fe}]} = \text{uncert.}_{[\text{V}/\text{H}]} - \text{uncert.}_{[\text{Fe}/\text{H}]}).$

4.3. Adopted abundances

Figure 12 presents the abundance patterns for all contaminating elements. Error bars were taken as the dispersion between the lines or the estimated [element/Fe] uncertainty, whichever is the largest (see Tables 8 and 9). The presence of a few ($\sim 4\%$) outliers can be noticed. For these stars, these abundances will not be used for the Eu and Th spectral syntheses. In these cases, the discrepant abundances will be substituted by the value they would have if they agreed with an exponential fit to the well behaved data points. One might wonder if the discrepant abundances would be a hint of chemical peculiarity. If this was true, one such star would exhibit peculiar abundances for all elements produced by one specific nucleosynthesis process, and this behaviour is not observed. Mark that the three stars which present discrepant abundances (HD 63 077, HD 76 932, and HD 203 608) are all metal-poor, with $[\text{Fe}/\text{H}] < -0.67$, and therefore more sensitive to noise and continuum placement errors. The Nd and V abundances of HD 196 378 and HD 203 608, which have no measured lines, were established this same way.

5. Eu and Th abundance determination

The Eu and Th abundance determination was carried out, for our sample stars, using a single absorption line for each element. The only acceptably strong Th line, which allows an accurate abundance determination, is the Th II line located at 4019.13 \AA . This line is, nevertheless, blended with many others, rendering imperative the use of spectral synthesis. One other line is often cited in the literature: a Th II line located at 4086.52 \AA . Unfortunately, although less contaminated than the line at 4019.13 \AA , it is too weak to be used.

Eu has only one adequately strong and uncontaminated line, located at 4129.72 \AA , available for abundance determinations. However, this line has a significantly non-gaussian profile by virtue of its HFS and isotope shift. Therefore, spectral synthesis is also required for this element. In stars of other spectral types and other luminosity classes (e.g. giants), it is possible to use other Th and Eu lines. This is, nonetheless, not true for our sample stars (late-F and G dwarfs/subgiants).

The code used to calculate the synthetic spectra was kindly made available to us by its developer, Monique Spite. This code calculates a synthetic spectrum based on a list of lines with their respective atomic parameters (log gf , and excitation potential of the lower level of the transition χ , in eV). We employed the same model atmospheres and partition functions used in the determination of atmospheric parameters and abundances of contaminating elements (Section 3.1). The only exception was for Th, whose partition functions were calculated by us, based on

Table 10. [element/H] abundance uncertainties for the standard stars. Last column contains the average uncertainty for each row, and the last row contains the average total uncertainty for the four standard stars.

Parameter	Δ Parameter	HD	[Fe/H]	[Ti/H]	[V/H]	[Cr/H]	[Mn/H]	[Co/H]	[Ni/H]	[Ce/H]	[Nd/H]	[Sm/H]	Average
T_{eff}	+27 K	160 691	+0.01	+0.02	+0.03	+0.02	+0.02	+0.02	+0.02	+0.00	+0.01	+0.01	+0.02 \pm 0.01
		22 484	+0.02	+0.02	+0.03	+0.02	+0.03	+0.03	+0.02	+0.01	+0.01	+0.01	+0.02 \pm 0.01
		63 077	+0.02	+0.02	+0.03	+0.01	+0.02	+0.02	+0.02	+0.01	+0.01	+0.01	+0.02 \pm 0.01
		59 984	+0.02	+0.02	+0.03	+0.02	+0.03	+0.02	+0.02	+0.01	+0.02	+0.01	+0.02 \pm 0.01
$\log g$	+0.02 dex	160 691	+0.00	+0.00	+0.00	+0.00	+0.00	+0.00	+0.00	+0.01	+0.01	+0.01	+0.00 \pm 0.00
		22 484	+0.00	+0.00	+0.01	+0.00	+0.00	+0.01	+0.00	+0.01	+0.01	+0.01	+0.01 \pm 0.01
		63 077	+0.00	+0.00	+0.00	+0.01	+0.00	+0.00	+0.00	+0.01	+0.01	+0.01	+0.00 \pm 0.01
		59 984	+0.00	+0.01	+0.00	+0.00	+0.00	+0.02	+0.00	+0.01	+0.01	+0.01	+0.01 \pm 0.01
ξ	$+0.05 \text{ km s}^{-1}$	160 691	-0.01	-0.02	+0.00	-0.01	-0.01	+0.00	-0.02	-0.01	-0.01	-0.01	-0.01 \pm 0.01
		22 484	-0.01	-0.01	-0.01	-0.02	+0.00	-0.01	-0.01	-0.01	-0.01	-0.01	-0.01 \pm 0.00
	$+0.23 \text{ km s}^{-1}$	63 077	-0.03	-0.03	-0.01	-0.04	+0.00	+0.00	+0.00	-0.02	-0.01	-0.01	-0.01 \pm 0.01
		59 984	-0.03	-0.03	+0.00	-0.04	+0.00	+0.00	-0.01	-0.01	-0.01	-0.01	-0.01 \pm 0.01
EW and $\log gf$	EW < 20 mÅ: +15%	160 691	+0.06	+0.07	+0.04	+0.07	+0.06	+0.03	+0.07	+0.04	+0.05	+0.04	+0.05 \pm 0.01
	EW > 20 mÅ: +5%	22 484	+0.06	+0.06	+0.08	+0.07	+0.03	+0.06	+0.06	+0.06	+0.08	+0.08	+0.06 \pm 0.02
	EW < 15 mÅ: +19%	63 077	+0.07	+0.05	+0.09	+0.08	+0.06	+0.09	+0.10	+0.10	+0.10	+0.10	+0.08 \pm 0.02
	EW > 15 mÅ: +5%	59 984	+0.06	+0.06	+0.10	+0.06	+0.05	+0.08	+0.08	+0.09	+0.10	+0.09	+0.08 \pm 0.02
[Fe/H]	Fe: +0.07 dex	160 691	+0.01	+0.01	+0.01	+0.01	+0.00	+0.01	+0.01	+0.03	+0.04	+0.04	+0.02 \pm 0.01
	Other elements:	22 484	+0.00	+0.01	+0.00	+0.01	+0.00	+0.01	+0.01	+0.03	+0.03	+0.03	+0.01 \pm 0.01
	+0.10 dex	63 077	+0.00	+0.01	+0.01	+0.01	+0.00	+0.00	+0.00	+0.02	+0.03	+0.01	+0.01 \pm 0.01
		59 984	+0.00	+0.01	+0.00	+0.01	+0.01	+0.01	+0.01	+0.02	+0.02	+0.01	+0.01 \pm 0.01
Total uncertainty		160 691	0.09	0.09	0.12	0.10	0.05	0.09	0.09	0.09	0.12	0.12	0.08 \pm 0.02
		22 484	0.09	0.10	0.06	0.10	0.09	0.05	0.10	0.07	0.08	0.07	0.10 \pm 0.02
		63 077	0.09	0.09	0.14	0.10	0.08	0.12	0.12	0.13	0.14	0.13	0.12 \pm 0.02
		59 984	0.11	0.08	0.13	0.12	0.09	0.13	0.14	0.14	0.15	0.14	0.11 \pm 0.02
Average total			0.10	0.09	0.11	0.11	0.08	0.10	0.11	0.11	0.12	0.12	0.10 \pm 0.03
			± 0.01	± 0.01	± 0.04	± 0.01	± 0.02	± 0.04	± 0.02	± 0.03	± 0.03	± 0.03	

Note: Contributions from EW and $\log gf$ are equal. The values which are presented correspond to *each* contribution, and not to the total of these two sources.

Therefore, they are taken in consideration *twice* when calculating the total uncertainties.

data from H. Holweger that was published as a *private communication* in MKB92. Irwin's data are too inaccurate, because for the singly and doubly ionised states of Th, he scales the partition functions along iso-electronic sequences from a lower mass element, due to lack of specific Th data. This resulted in values much lower than those of Holweger, which were calculated by summing a large number of Th atomic levels.

5.1. Europium

5.1.1. Spectral synthesis

The list of lines used for calculation of the synthetic spectrum of the Eu region was based on the line lists of the Vienna Atomic Line Database – VALD (Kupka et al. 1999). Initially, we took all lines found between 4128.4 Å and 4130.4 Å. The first cut eliminated all lines of elements ionised two or more times, and all lines with lower-level excitation potential greater than 10 eV, since these lines are unobservable in the photospheres of stars with effective temperatures as low as those in our sample. As a next step, we calculated synthetic spectra for the four stars with the most extreme effective temperatures and metallicities in our sample (HD 22 484, HD 59 984, HD 63 077, and HD 203 608) using laboratory $\log g f$ values, and the atmospheric parameters and abundances previously obtained. Lines with EWs lower than 0.01 mÅ in these four stars were removed. The Sc I line located at 4129.750 Å, cited as important by Mashonkina & Gehren (2000), presents negligible EW in all four standard stars. 23 Ti, V, Cr, Fe, Co, Nb, Ce, Pr, Nd, Sm, and Dy lines were kept, besides the Eu line itself. Adopted wavelengths were taken from the VALD list (Bard & Kock 1994; Kurucz 1993, 1994; Whaling 1983; Wickliffe et al. 1994). To improve the fits further, three artificial Fe I lines were added as substitutes for unknown blends (Lawler et al. 2001; Mashonkina & Gehren 2000); the influence of these artificial lines in the obtained Eu abundances is nevertheless small, as they are located relatively far from the center of the Eu II line. The final list is presented in Table 11.

In the spectral synthesis calculations, the Eu II line was substituted by its HFS components, calculated by us using Casimir's equation (Casimir 1963), and HFS laboratory data from Becker et al. (1993), Broström et al. (1995), Villemoes & Wang (1994), and Möller et al. (1993). Isotope shift was taken into account, using data from Broström et al. (1995) and the solar abundance isotopic ratio $\varepsilon(^{151}\text{Eu})/\varepsilon(^{153}\text{Eu}) = 1.00 \pm 0.29$ (Lawler et al. 2001). The solar value was used for all stars because there are strong indications that it is not metallicity-dependent, since several works dealing with r-process nucleosynthesis in very-metal-poor halo stars find similar results (Pfeiffer et al. 1997; Cowan et al. 1999; Sneden et al. 2002; Aoki et al. 2003).

We adopted a projected rotation velocity for the integrated solar disk $v \sin i = 1.8 \text{ km s}^{-1}$ (Mashonkina 2000; Mashonkina & Gehren 2000). The width of the gaussian profile convolved to the synthetic spectrum to take macroturbulence and instrumental broadenings into account was obtained by fitting the Fe II located at 4128.742 Å, which is sufficiently isolated for this purpose (Woolf et al. 1995; Koch & Edvardsson

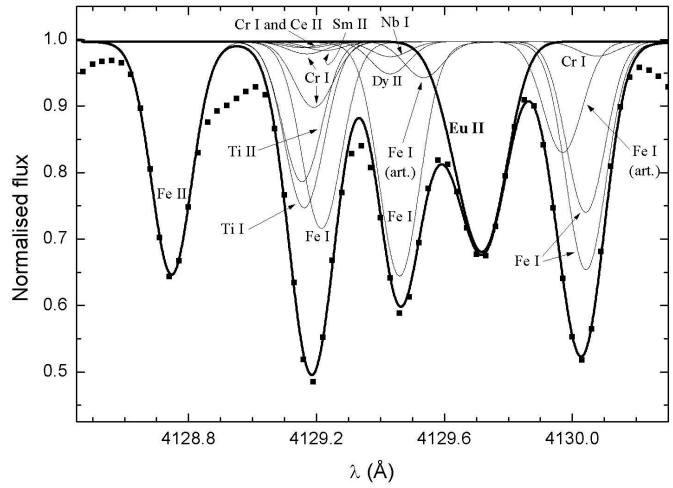


Fig. 13. Synthesized spectral region for the Eu II line at 4129.72 Å, for the Sun. The two thick lines represent the total synthetic spectrum and the Eu II line. The thin lines represent the most dominant lines in the region, including two artificial Fe I lines. Points are the observed FEROS solar spectrum.

2002). Solar $\log g f$ were obtained by keeping abundances fixed at their solar values (Grevesse & Sauval 1998), and fitting the observed solar spectrum. Only the stronger Ti, Cr, and Fe lines had their $\log g f$ adjusted. For the Eu II line, we adopted a fixed $\log g f$ from Komarovskii (1991); this value was distributed among the HFS components according to relative intensities calculated by White & Eliason, tabulated in Condon & Shortley (1967). The other, weaker lines had their $\log g f$ kept at their laboratory values adopted from the VALD list (Kurucz 1993, 1994; Wickliffe et al. 1994). As we kept the Eu $\log g f$ fixed, we allowed its abundance to vary. The complete solar spectrum fit procedure was carried out iteratively because it requires alternate gaussian profile adjustments (which modify the *shape* of the lines) and $\log g f$ adjustments (which modify the *EWs* of the lines). The solar $\log g f$ and gaussian profile determination was accomplished independently for the two sources of Eu spectra used, leading to different Eu solar abundances ($\log \varepsilon(\text{Eu})_{\odot} = +0.37$ and $+0.47$ for the CES and FEROS, respectively). The stellar [Eu/H] abundance ratios, used in this work in lieu of the absolute abundances, were obtained by subtracting the appropriate solar value from the stellar absolute abundances ($[\text{Eu}/\text{H}] = \log \varepsilon(\text{Eu})_{\text{star}} - \log \varepsilon(\text{Eu})_{\odot}$). Figure 13 presents the observed and synthetic solar spectrum in the Eu region. The strongest lines that compose the total synthetic spectrum are presented independently.

For the Eu synthesis in the sample stars, we kept the abundances of all elements other than Eu fixed at the values determined using EWs, in Sect. 4. Small adjustments were allowed only to the abundances of Ti, Cr, and Fe, in order to improve the fit. The adjustments were kept within the uncertainties of the abundances of these elements – see Sect. 4. The abundances of elements for which we did not measure any EW were determined scaling the solar abundances, following elements produced by the same nucleosynthetic processes. We chose to scale the Sm abundances as well, even though they were deter-

Table 11. Line list used in the spectral synthesis of the Eu II line at 4129.72 Å.

λ (Å)	Element	χ (eV)	$\log g f_{\text{CES}}$	$\log g f_{\text{FEROS}}$	$\log g f$ source	Obs.
4128.742	Fe II	2.580	-3.832	-3.554	solar fit	
4129.000	Cr I	4.210	-2.603	-2.603	VALD	
4129.040	Ru I	1.730	-1.030	-1.030	VALD	
4129.147	Pr II	1.040	-0.100	-0.100	VALD	
4129.159	Ti II	1.890	-2.330	-2.210	solar fit	
4129.166	Ti I	2.320	+0.131	+0.251	solar fit	
4129.165	Cr I	3.010	-1.948	-1.948	VALD	
4129.174	Ce II	0.740	-0.901	-0.901	VALD	
4129.196	Cr I	2.910	-1.374	-1.254	solar fit	
4129.220	Fe I	3.420	-2.280	-2.160	solar fit	
4129.220	Sm II	0.250	-1.123	-1.123	VALD	
4129.425	Dy II	0.540	-0.522	-0.522	VALD	
4129.426	Nb I	0.090	-0.780	-0.780	VALD	
4129.461	Fe I	3.400	-2.180	-1.920	solar fit	
4129.530	Fe I	3.140	-3.425	-3.455	solar fit	artificial
4129.610	Fe I	3.500	-3.700	-3.730	solar fit	artificial
4129.643	Ti I	2.240	-1.987	-1.987	VALD	
4129.657	Ti I	2.780	-2.297	-2.297	VALD	
4129.721	Eu II	0.000	+0.173	+0.173	Komarovskii (1991)	HFS
4129.817	Co I	3.810	-1.808	-1.808	VALD	
4129.837	Nd II	2.020	-0.543	-0.543	VALD	
4129.965	Fe I	2.670	-3.390	-3.290	solar fit	artificial
4129.994	V I	2.260	-1.769	-1.769	VALD	
4130.037	Fe I	1.560	-4.195	-4.030	solar fit	
4130.038	Fe I	3.110	-2.385	-2.225	solar fit	
4130.068	Fe I	3.700	-3.763	-3.763	VALD	
4130.073	Cr I	2.910	-1.971	-1.971	VALD	

References: see text.

mined by us, because our results for this element exhibit high scatter and absence of well-defined behaviour (see Fig. 12). Sm and Dy abundances were obtained following Eu (produced mainly by r-process, according to Burris et al. 2000); Nb, Rb, and Pr were obtained following Nd (produced by both r-process and s-process, also according to Burris et al. 2000). Mark that the influence of these lines is marginal, since they are weak and are not close to the Eu line. Projected rotation velocities $v \sin i$ and macroturbulence and instrumental broadening gaussian profiles were determined by fitting the Fe II line at 4128.742 Å, like done with the solar spectrum.

Stars observed more than once had their spectra analysed independently, and the results were averaged. Abundances obtained with the different spectra of one object presented a maximum variation of 0.02 dex. Examples of spectral syntheses can be seen in Fig. 14 for the two stars with extreme Eu abundances that were observed with both FEROS and CES (HD 63 077 and HD 160 691). Note the effect of CES spectra higher sampling, which better puts the asymmetric profile of the Eu II line in evidence.

Eu abundances obtained using CES and FEROS spectra are compared in Fig. 15. A linear fit was calculated, and the resulting relation was used to convert FEROS results into the CES system. This way, we ended up with two sets of Eu abundances: one totally homogeneous, obtained with FEROS spectra, and one obtained partially with CES spectra and partially with corrected-into-CES-system FEROS spectra. We plotted a [Eu/Fe] vs. [Fe/H] diagram for both sets of abundances, pre-

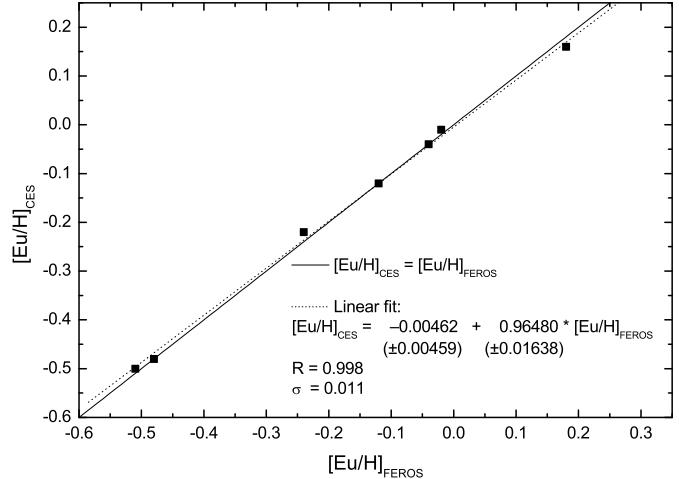


Fig. 15. Comparison between Eu abundances determined using CES and FEROS spectra. Solid line is the identity. Dotted line is a linear fit, whose parameters are shown in the figure.

sented in Fig. 16. Linear fits calculated for each set show that the CES abundances present a lower scatter σ , and for this reason the CES results were adopted for all subsequent analyses.

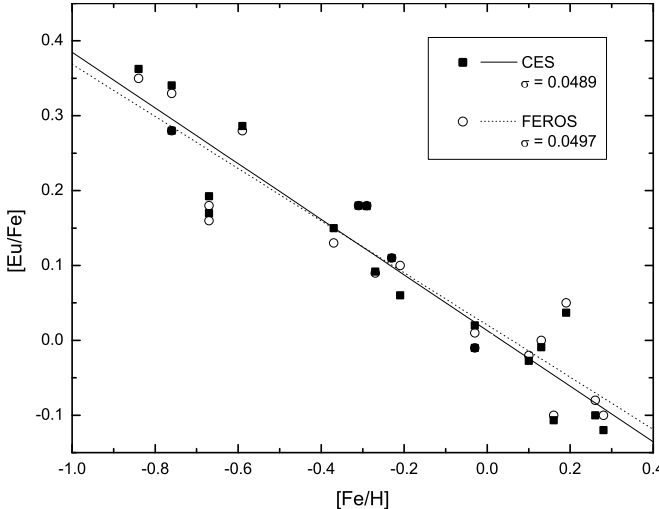


Fig. 16. [Eu/Fe] vs. [Fe/H] diagram for all sample stars. Abundances obtained with CES and FEROS spectra are presented. The Sun is not included in the comparison, since its abundance is always equal to zero by definition. Solid and dotted lines are linear fits to these two data sets, whose scatters are shown in the figure. Mark that data from the CES are slightly better than those from FEROS.

5.1.2. Uncertainty assessment

[Eu/H] abundance uncertainties were estimated with a procedure identical to the one used for the abundances of contaminating elements determined with EWs, thoroughly described in Sect. 4.2. It consists basically of varying the atmospheric parameters and continuum position independently, by an amount equal to their uncertainties, and recalculating the synthetic spectra. Total uncertainties are obtained by RMS of the individual sources of uncertainty. We chose four stars as standards for the assessment, with extreme effective temperatures and metallicities: HD 160 691 (cool and metal-rich), HD 22 484 (hot and metal-rich), HD 63 077 (cool and metal-poor), and HD 203 608 (hot and metal-poor) – Fig. 10.

Continuum placement is the preponderant source of Eu abundance uncertainty. The placement uncertainty itself is higher for metal-rich stars, as these present stronger absorption lines, lowering the apparent continuum which restricts the choice of good normalisation windows. To estimate the influence of continuum placement uncertainties, we multiplied the spectral flux of the metal-rich standard stars by 0.98, and that of the metal-poor standard stars by 0.99, and recalculated the synthetic spectra.

Table 13 presents the [Eu/H], [Eu/Fe], [Th/H], [Th/Fe], and [Th/Eu] uncertainties for each standard star. Metallicity and continuum placement clearly dominate. Microturbulence velocity variations have no effect in the [Eu/H] abundances. This happens because the HFS broadens the line so much that it becomes nearly unsaturated, as found by Woolf et al. (1995, WTL95), Lawler et al. (2001) and Koch & Edvardsson (2002, KE02). [Element/Fe] uncertainties were obtained simply by subtracting the [Fe/H] uncertainty from the [element/H] value (e.g., $\text{uncert.}_{[\text{Eu}/\text{Fe}]} = \text{uncert.}_{[\text{Eu}/\text{H}]} - \text{uncert.}_{[\text{Fe}/\text{H}]}$). Total uncer-

tainties for the other sample stars were obtained by weighted average of the standard stars values, using as weight the reciprocal of the distance of the star to each standard star, in the T_{eff} vs. [Fe/H] plane; this procedure is identical to the one used for the uncertainties of contaminating elements (Sect. 4.2). Table 14 presents the final [Eu/H], [Th/H], and [Th/Eu] abundance ratios, for all sample stars, along with their respective uncertainties relative to H and Fe.

Non-LTE effects in the abundances obtained with the Eu II line at 4129.72 Å have been calculated by Mashonkina & Gehren (2000). In the line formation layers, the ground state was found to be slightly underpopulated, and the excited level overpopulated. As a consequence, our results would show a small difference if our method employed absolute abundances. But since we employ a differential analysis, these differences cancel each other partially, becoming negligible (WTL95 and KE02).

5.1.3. Comparison with literature results

We conducted a painstaking search in the literature for works with Eu abundances, and selected WTL95 and KE02 as the ones with the most careful determinations for disk stars, as well as a sizable sample of high statistic significance. Their sample is composed of a subset from Edvardsson et al. (1993), and they use the same atmospheric parameters (obtained from Strömgren photometric calibrations). The Eu abundances were determined by spectral synthesis using the same line we used, with a procedure fundamentally identical to ours. KE02 merged their database with that from WTL95 by means of a simple linear conversion, obtained by intercomparison. We used this merged set of abundances to compare to our results.

Figure 17 presents a [Eu/H] vs. [Fe/H] diagram with our results and those from WTL95 and KE02. Both data sets exhibit the same behaviour, but our results present scatter 36% lower than those of WTL95 and KE02, even though our sample is 6 times smaller than theirs (linear fits result in $\sigma_{\text{our work}} = 0.050$ and $\sigma_{\text{WTL95/KE02}} = 0.078$). The lower scatter of our results is a consequence of improvements introduced in our analysis, like the use of atmospheric parameters obtained by us through the detailed and totally self-consistent spectroscopic analysis carried out in Sect. 3. WTL95 and KE02 demonstrated, using Monte Carlo simulations of observational errors, that the observed scatter is not real, but mainly a result of observational, analytical, and systematic errors.

5.2. Thorium

5.2.1. Spectral synthesis

The list of lines used for calculation of the synthetic spectrum of the Th region was constructed following the same procedure used for the Eu analysis. 14 V, Mn, Fe, Co, Ni, W, Ce, and U lines were kept, besides the Th line itself. Adopted wavelengths were taken from the VALD list (Bard & Kock 1994; Kurucz 1993, 1994; Whaling 1983), with the exception of the Fe I line at 4019.043 Å, Ni I at 4019.067 Å, and Th II at 4019.130 Å, determined in laboratory by Learner et al. (1991) with a preci-

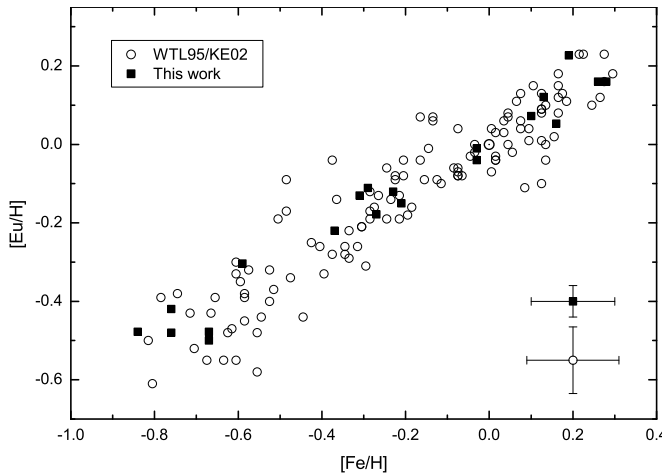


Fig. 17. [Eu/H] vs. [Fe/H] diagram for our sample stars and those from WTL95 and KE02. Average error bars for the two data sets are provided in the lower right corner. Note that the behaviour of both data sets is similar, but that our abundances present considerably lower scatter.

sion higher than 0.0005 \AA . The Co I lines were substituted by their HFSs components, calculated by us using Casimir's equation, and HFS laboratory data from Childs & Goodman (1968), Guthöhrlein & Keller (1990), Pickering & Thorne (1996), and Pickering (1996). To improve the fits further, one artificial Fe II line was added as substitute for unknown blends (MKB92; François et al. 1993); the influence of this artificial line in the obtained Th abundances is nevertheless small, as it is located relatively far from the center of the Th II line. The final list is presented in Table 12.

The width of the gaussian profile used to take macroturbulence and instrumental broadenings into account was obtained by fitting the Co I lines located at 4019.293 \AA and 4019.297 \AA . Solar $\log gf$ were obtained by keeping abundances fixed at their solar values (Grevesse & Sauval 1998), and fitting the observed solar spectrum. Only the stronger Mn, Fe, Ce, and Ni lines had their $\log gf$ adjusted. For the Th II line, we adopted a fixed $\log gf$ from Nilsson et al. (2002); for the Co I lines we adopted fixed $\log gf$ from Lawler et al. 1990 (4019.132 \AA) and VALD (4019.293 \AA and 4019.297 \AA , Kurucz 1994). The other, weaker lines had their $\log gf$ kept at their laboratory values adopted from the VALD list (Kurucz 1993, 1994). As we kept the Th $\log gf$ fixed, we allowed its abundance to vary. The complete solar spectrum fit procedure was carried out iteratively because it requires alternate gaussian profile adjustments (which modify the *shape* of the lines) and $\log gf$ adjustments (which modify the *EWs* of the lines). The solar $\log gf$ and gaussian profile determination was accomplished independently for each telescope used, leading to slightly different Th solar abundances ($\log \varepsilon(\text{Th})_{\odot} = +0.03$ and $+0.04$ for the 3.60 m and CAT, respectively). As with Eu, the stellar $[\text{Th}/\text{H}]$ abundance ratios were obtained by subtracting the appropriate solar value from the stellar absolute abundances ($[\text{Th}/\text{H}] = \log \varepsilon(\text{Th})_{\text{star}} - \log \varepsilon(\text{Th})_{\odot}$). Figure 18 presents the observed and synthetic solar spectrum in the Th region. The

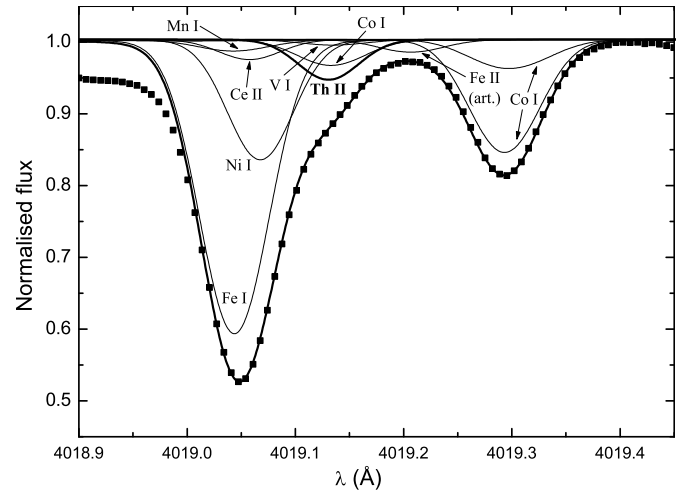


Fig. 18. Synthesized spectral region for the Th II line at 4019.13 \AA , for the Sun. The two thick lines represent the total synthetic spectrum and the Th II line. The thin lines represent the most dominant lines in the region, including an artificial Fe II line. Points are the observed CES solar spectrum, obtained with the 3.60 m telescope.

strongest lines that compose the total synthetic spectrum are presented independently.

For the Th synthesis in the sample stars, we kept the abundances of all elements other than Th fixed at the values determined using EWs, in Sect. 4. Small adjustments were allowed only to the abundances of Mn, Fe, Ce, and Ni, in order to improve the fit. The adjustments were kept within the uncertainties of the abundances of these elements – see Sect. 4. The W abundances, for which we did not measure any EW, were determined scaling the solar abundances, following the Fe abundances. The U abundances were estimated from a simplifying hypothesis that the $[\text{U}/\text{H}]$ stellar abundance at the time of formation is independent of metallicity. We allied this hypothesis to a simple linear age-metallicity relation, in which a star with $[\text{Fe}/\text{H}] = -1.00$ is 10 Gyr old, and one with $[\text{Fe}/\text{H}] = +0.00$ is 4.57 Gyr old, i.e., $\text{age(Gyr)} = 4.57 - 5.43 [\text{Fe}/\text{H}]$. Given the known ^{238}U half-life $t_{1/2} = 4.46 \text{ Gyr}$, we reach a relation $[\text{U}/\text{H}] = -0.50 + 0.37 [\text{Fe}/\text{H}]$. Mind that the W and U lines have only a small influence on the final Th derived by the analysis, since they are weak (with $\text{EW} < 0.2 \text{ m\AA}$ for the metal-richest stars) and are not close to the Th line. We employed the projected rotation velocities $v \sin i$ determined in the Eu analysis, and the macroturbulence and instrumental broadening gaussian profiles were obtained by fitting the Co I lines at 4019.293 \AA and 4019.297 \AA , like done with the solar spectrum.

Stars observed more than once had their spectra analysed individually, and the results were averaged. Different spectra for each star presented a 0.02 dex maximum variation. Examples of spectral syntheses can be seen in Fig. 19 for the two stars with extreme Th abundances that were observed with both 3.60 m and CAT (HD 20 766 and HD 128 620). Mark that, due to problems that degraded the resolving power of spectra obtained with the 3.60 m telescope, these are almost identical to the ones obtained with the CAT.

Table 12. Line list used in the spectral synthesis of the Th II line at 4019.13 Å.

λ (Å)	Element	χ (eV)	$\log g f_{3.60\text{ m}}$	$\log g f_{\text{CAT}}$	$\log g f$ source	Obs.
4018.986	U II	0.04	-1.391	-1.391	VALD	
4018.999	Mn I	4.35	-1.497	-1.497	VALD	
4019.036	V II	3.75	-2.704	-2.704	VALD	
4019.042	Mn I	4.67	-1.031	-1.026	solar fit	
4019.043	Fe I	2.61	-3.150	-3.145	solar fit	
4019.057	Ce II	1.01	-0.470	-0.445	solar fit	
4019.067	Ni I	1.94	-3.404	-3.329	solar fit	
4019.130	Th II	0.00	-0.228	-0.228	Nilsson et al. (2002)	
4019.132	Co I	2.28	-2.270	-2.270	Lawler et al. (1990)	HFS
4019.134	V I	1.80	-1.300	-1.300	VALD	
4019.206	Fe II	3.00	-5.380	-5.425	solar fit	artificial
4019.228	W I	0.41	-2.200	-2.200	VALD	
4019.293	Co I	0.58	-3.232	-3.232	VALD	HFS
4019.297	Co I	0.63	-3.769	-3.769	VALD	HFS

References: see text.

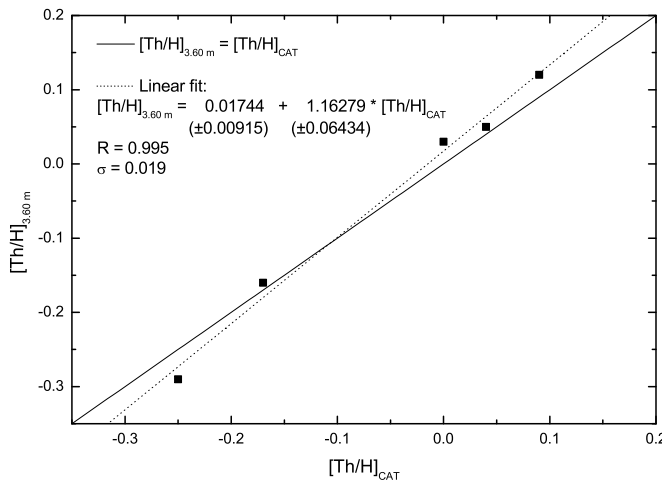


Fig. 20. Comparison between Th abundances determined using CES spectra obtained with the CAT and with the 3.60 m. Solid line is the identity. Dotted line is a linear fit, whose parameters are shown in the figure.

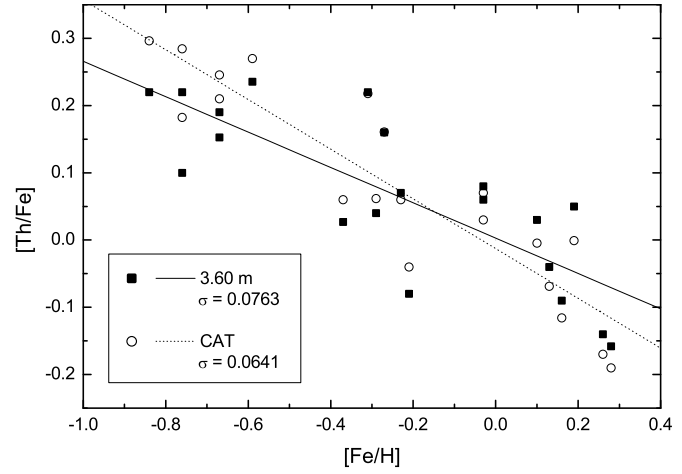


Fig. 21. [Th/Fe] vs. [Fe/H] diagram for all sample stars. Abundances determined using CES spectra obtained with the CAT and the 3.60 m are presented. The Sun is not included in the comparison, since its abundance is always equal to zero by definition. Solid and dotted lines are linear fits to these two data sets, whose scatters are shown in the figure. Mark that data from the CAT are better than those from 3.60 m.

Th abundances determined using spectra obtained with the 3.60 m and CAT are compared in Fig. 20. A linear fit was calculated, and the resulting relation was used to convert 3.60 m results into the CAT system, and vice versa. This way, we ended up with two sets of Th abundances: one obtained partially with 3.60 m spectra and partially with corrected-into-3.60-m-system CAT spectra, and one that is just the opposite, obtained partially with CAT spectra and partially with corrected-into-CAT-system 3.60 m spectra. We plotted a [Th/Fe] vs. [Fe/H] diagram for both sets of abundances, presented in Fig. 21. Linear fits calculated for each set show that the CAT abundances present a lower scatter σ , and for this reason the CAT results were adopted for all subsequent analyses. Thus, our adopted Eu and Th were obtained in one and the same system, related to one single instrument (CES) and telescope (CAT), reinforcing the homogeneity of the analysis.

5.2.2. Uncertainty assessment

[Th/H] abundance uncertainties were obtained with a procedure identical to the one used for Eu. Table 13 contains the results of the Th uncertainty analysis for the four standard stars, and Table 14 contains the abundances for all sample stars, with their respective uncertainties. Dependence of Th abundances on atmospheric parameters is similar to Eu, but exhibit 3 to 5 times higher sensitivity to continuum placement variations. This results from the much lower EW of the Th line, which ranges from 1 mÅ to 8 mÅ for our sample stars, whereas Eu ranges from 20 mÅ to 90 mÅ. Furthermore, the Eu line is practically isolated from contaminations, while the Th line is located in the red wing of a feature composed of strong Mn, Fe, Ce, and Ni lines, and is blended with one V I and one Co I line

Table 13. [Eu/H], [Eu/Fe], [Th/H], [Th/Eu], and [Th/Eu] abundance uncertainties for the standard stars.

Parameter	Δ Parameter	HD	[Eu/H]	[Eu/Fe]	[Th/H]	[Th/Fe]	[Th/Eu]
T_{eff}	+27 K	160 691	+0.01	+0.00	+0.00	-0.01	-0.01
		22 484	+0.01	-0.01	+0.01	-0.01	+0.00
		63 077	+0.01	-0.01	+0.01	-0.01	+0.00
		203 608	+0.02	+0.00	+0.01	-0.01	-0.01
$\log g$	+0.02 dex	160 691	+0.01	+0.01	+0.01	+0.01	+0.00
		22 484	+0.01	+0.01	+0.01	+0.01	+0.00
		63 077	+0.01	+0.01	+0.01	+0.01	+0.00
		203 608	+0.01	+0.01	+0.01	+0.01	+0.00
ξ	+0.05 km s ⁻¹	160 691	+0.00	+0.01	+0.00	+0.01	+0.00
		22 484	+0.00	+0.01	+0.00	+0.01	+0.00
		63 077	+0.00	+0.03	+0.00	+0.03	+0.00
		203 608	+0.00	+0.03	+0.00	+0.03	+0.00
[Fe/H]	+0.10 dex	160 691	+0.03	+0.02	+0.04	+0.03	+0.01
		22 484	+0.02	+0.02	+0.03	+0.03	+0.01
		63 077	+0.02	+0.02	+0.02	+0.02	+0.00
		203 608	+0.01	+0.01	+0.02	+0.02	+0.01
Continuum	+2%	160 691	+0.02	-0.04	+0.09	+0.03	+0.07
		22 484	+0.03	-0.03	+0.10	+0.04	+0.07
		63 077	+0.02	-0.05	+0.11	+0.04	+0.09
		203 608	+0.03	-0.03	+0.14	+0.08	+0.11
Total uncertainty		160 691	0.04	0.05	0.10	0.05	0.07
		22 484	0.04	0.04	0.11	0.05	0.07
		63 077	0.03	0.06	0.11	0.06	0.09
		203 608	0.04	0.04	0.14	0.09	0.11

Table 14. [Eu/H], [Th/H], and [Th/Eu] abundance ratios for all sample stars, with their respective uncertainties relative to H and Fe.

HD	[Eu/H]	uncert. _[Eu/H]	uncert. _[Eu/Fe]	[Th/H]	uncert. _[Th/H]	uncert. _[Th/Fe]	[Th/Eu]	uncert. _[Th/Eu]
2151	-0.04	0.04	0.05	+0.00	0.11	0.06	+0.04	0.08
9562	+0.05	0.04	0.05	+0.04	0.11	0.06	-0.01	0.08
16 417	+0.12	0.04	0.05	+0.06	0.11	0.06	-0.06	0.08
20 766	-0.15	0.04	0.05	-0.25	0.11	0.06	-0.10	0.08
20 807	-0.12	0.04	0.05	-0.17	0.11	0.06	-0.05	0.08
22 484	-0.01	0.04	0.04	+0.04	0.11	0.05	+0.05	0.07
22 879	-0.42	0.04	0.05	-0.58	0.12	0.07	-0.16	0.09
30 562	+0.23	0.04	0.05	+0.19	0.11	0.06	-0.04	0.08
43 947	-0.18	0.04	0.05	-0.11	0.12	0.06	+0.07	0.08
52 298	-0.13	0.04	0.04	-0.09	0.12	0.06	+0.04	0.09
59 984	-0.48	0.04	0.05	-0.42	0.12	0.07	+0.06	0.09
63 077	-0.48	0.03	0.06	-0.48	0.11	0.06	+0.00	0.09
76 932	-0.48	0.04	0.05	-0.54	0.12	0.07	-0.06	0.09
102 365	-0.11	0.04	0.05	-0.23	0.11	0.06	-0.12	0.08
128 620	+0.16	0.04	0.05	+0.09	0.11	0.06	-0.07	0.08
131 117	+0.07	0.04	0.05	+0.10	0.11	0.06	+0.03	0.08
160 691	+0.16	0.04	0.05	+0.09	0.10	0.05	-0.06	0.07
196 378	-0.22	0.04	0.04	-0.31	0.12	0.07	-0.10	0.09
199 288	-0.30	0.03	0.05	-0.32	0.11	0.06	-0.02	0.09
203 608	-0.50	0.04	0.04	-0.46	0.14	0.09	+0.04	0.11

that, depending on the metallicity of the star, has EW comparable to the Th itself.

5.2.3. Comparison with literature results

There are only two works available in the literature in which Th abundances have been determined for Galactic disk stars:

da Silva et al. (1990) and MKB92. In the classic work of Butcher (1987), which was the first to propose the use of stellar Th abundances as chronometers, the ratio between the EWs of Th and Nd is adopted as an estimate of [Th/Nd], but no independent Th abundances are derived. We did not compare our results to those from da Silva et al. because only preliminary data is presented for a small sample of four stars.

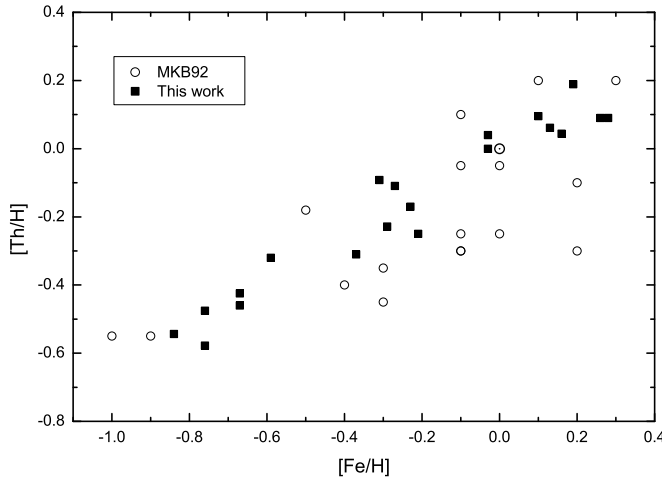


Fig. 22. [Th/H] vs. [Fe/H] diagram for our sample stars and those from MKB92. Note that the behaviour of both data sets is similar, but that our abundances present considerably lower scatter.

MKB92 is a re-analysis of the Butcher (1987) data, with the same stellar sample and spectra, but making use of more up-to-date model atmospheres and more detailed spectral syntheses. Unfortunately, MKB92 do not present a detailed Th abundance uncertainty analysis. The authors investigated the influence of effective temperature, surface gravity and continuum placement variations, but overlooked metallicity and microturbulence velocity. No estimate of total uncertainty is presented. Therefore, we decided not to include error bars in Fig. 22, which depicts [Th/H] vs. [Fe/H] for our results and those from MKB92. The two data sets exhibit a similar behaviour, but our results present scatter 61% lower than those of MKB92 (from linear fits we get $\sigma_{\text{our work}} = 0.064$ and $\sigma_{\text{MKB92}} = 0.165$). The lower scatter of our results is a consequence of many enhancements introduced in our analysis, like the use of homogeneous and precise atmospheric parameters obtained by us, while MKB92 used multiple literature sources, and refinements in the spectral synthesis.

6. Conclusions

Homogenous, fully self-consistent atmospheric parameters, and their respective uncertainties, have been obtained for all sample stars. The use of two different and internally homogeneous criteria for effective temperature determination allowed us to achieve a very low uncertainty (27 K) for this important parameter. Uncertainties of the other parameters were also found to be adequate for our needs.

Abundances of the elements that contaminate the Th II and Eu II spectral regions – Ti, V, Cr, Mn, Co, Ni, Ce, Nd, and Sm – have been determined by detailed spectroscopic analysis, relative to the Sun, using EWs. For the elements with meaningful HFSs (V, Mn, and Co), it has been taken into account. A thorough estimation of the uncertainties has been carried out. The average [element/H] uncertainty – (0.10 ± 0.02) dex – was found to be satisfactorily low.

Eu and Th abundances have been determined for all sample stars using spectral synthesis of the Eu II line at 4129.72 Å and the Th II line at 4019.13 Å. Comparison of our results with the literature shows that our analysis yielded a similar behaviour, but with considerably lower scatters (36% lower for Eu, and 61% lower for Th). The [Th/Eu] abundance ratios thus obtained were used to determine the age of the Galactic disk in Paper II.

Acknowledgements. This paper is based on the PhD thesis of one of the authors (del Peloso 2003). The authors wish to thank the staff of the Observatório do Pico dos Dias, LNA/MCT, Brazil and of the European Southern Observatory, La Silla, Chile. The support of Martin Kürster (Thüringer Landessternwarte Tautenburg, Germany) during the observations with the ESO's 3.60 m telescope was greatly appreciated. EFP acknowledges financial support from CAPES/PROAP and FAPERJ/FP (grant E-26/150.567/2003). LS thanks the CNPq, Brazilian Agency, for the financial support 453529.0.1 and for the grants 301376/86-7 and 304134-2003.1. GFPM acknowledges financial support from CNPq/Conteúdos Digitais, CNPq/Institutos do Milênio/MEGALIT, FINEP/PRONEX (grant 41.96.0908.00), and FAPESP/Temáticos (grant 00/06769-4).

References

- Aoki, W., Honda, S., Beers, T. C., & Sneden, C. 2003, ApJ, 586, 506
- Axer, M., Fuhrmann, K., & Gehren, T. 1994, A&A, 291, 895
- Bard, A. & Kock, M. 1994, A&A, 282, 1014
- Becker, O., Enders, K., Werth, G., & Dembczynski, J. 1993, Phys. Rev. A, 48, 3546
- Blackwell, D. E., Lynas-Gray, A. E., & Petford, A. D. 1991, A&A, 245, 567
- Blackwell, D. E., Petford, A. D., & Shallis, M. J. 1980, A&A, 82, 249
- Broström, L., Mannervik, S., Royen, P., & Wänström, A. 1995, Phys. Scr, 51, 330
- Brown, J. A. & Wallerstein, G. 1992, AJ, 104, 1818
- Burris, D. L., Pilachowski, C. A., Armandroff, T. E., et al. 2000, ApJ, 544, 302
- Buser, R., Rong, J., & Karaali, S. 1998, A&A, 331, 934
- Butcher, H. R. 1987, Nature, 328, 127
- Casimir, H. B. G. 1963, On the Interaction Between Atomic Nuclei and Electrons (San Francisco: Freeman)
- Castro, S., Porto de Mello, G. F., & da Silva, L. 1999, MNRAS, 305, 693
- Cayrel, R. & Traving, G. 1960, Zeitschrift fur Astrophysics, 50, 239
- Cayrel de Strobel, G. & Bentolila, C. 1989, A&A, 211, 324
- Cayrel de Strobel, G., Soubiran, C., & Ralite, N. 2001, A&A, 373, 159
- Charbonnel, C., Meynet, G., Maeder, A., & Schaerer, D. 1996, A&AS, 115, 339 (Gen92/96)
- Charbonnel, C., Meynet, G., Maeder, A., Schaller, G., & Schaerer, D. 1993, A&AS, 101, 415 (Gen92/96)
- Chen, Y. Q., Nissen, P. E., Zhao, G., Zhang, H. W., & Benoni, T. 2000, A&AS, 141, 491
- Childs, W. J. & Goodman, L. S. 1968, Physical Review, 170, 50

Condon, E. U. & Shortley, G. H. 1967, *The Theory of Atomic Spectra* (Cambridge: Cambridge University Press)

Cowan, J. J., Pfeiffer, B., Kratz, K.-L., et al. 1999, *ApJ*, 521, 194

Cowley, C. R., Allen, M. S., & Aikman, G. C. L. 1975, *Nature*, 258, 311

Cowley, C. R. & Castelli, F. 2002, *A&A*, 387, 595

Crawford, D. L., Barnes, J. V., Faure, B. Q., & Golson, J. C. 1966, *AJ*, 71, 709

Crawford, D. L., Barnes, J. V., & Golson, J. C. 1970, *AJ*, 75, 624

da Silva, L. 1975, *A&A*, 41, 287

da Silva, L., de La Reza, R., & de Magalhaes, S. D. 1990, in *Proceedings of the Fifth IAP Workshop, Astrophysical Ages and Dating Methods*. Editors: E. Vangioni-Flam, M. Casse, J. Audouze, J. Tran Thanh Van. Publisher: Editions Frontières., Gif sur Yvette, 419

da Silva, L. & Porto de Mello, G. F. 2000, in *IAU Symposium*, Vol. 198, 495

da Silva, R. O. 2000, Senior Thesis, Observatório do Valongo/UFRJ, Rio de Janeiro, Brazil

Dehnen, W. & Binney, J. J. 1998, *MNRAS*, 298, 387

del Peloso, E. F. 2003, PhD thesis, Observatório Nacional/MCT, Rio de Janeiro, Brazil

del Peloso, E. F., da Silva, L., & Arany-Prado, L. I. 2005a, *A&A*, accepted for publication, available at <http://arxiv.org/abs/astro-ph/0411699> (Paper II)

del Peloso, E. F., da Silva, L., & Porto de Mello, G. F. 2000, *A&A*, 358, 233

del Peloso, E. F., da Silva, L., Porto de Mello, G. F., & Cunha, K. 2005b, *A&A*, to be submitted

di Benedetto, G. P. 1998, *A&A*, 339, 858

Edvardsson, B., Andersen, J., Gustafsson, B., et al. 1993, *A&A*, 275, 101

Fehrenbach, C. 1961, *Journal des Observateurs*, 44, 233

François, P., Spite, M., & Spite, F. 1993, *A&A*, 274, 821

Fuhrmann, K. 1998, *A&A*, 338, 161

Fuhrmann, K., Axer, M., & Gehren, T. 1993, *A&A*, 271, 451

Fuhrmann, K., Axer, M., & Gehren, T. 1994, *A&A*, 285, 585

Furenlid, I. & Meylan, T. 1990, *ApJ*, 350, 827

Gehren, T. 1981, *A&A*, 100, 97

Gratton, R. G., Carretta, E., & Castelli, F. 1996, *A&A*, 314, 191

Grevesse, N. & Sauval, A. J. 1998, *Space Science Reviews*, 85, 161

Grønbech, B. & Olsen, E. H. 1976, *A&AS*, 25, 213

Grønbech, B. & Olsen, E. H. 1977, *A&AS*, 27, 443

Guthöhrlein, G. H. & Keller, H. P. 1990, *Z. Phys. D*, 17, 181

Habets, G. M. H. J. & Heintze, J. R. W. 1981, *A&AS*, 46, 193

Hartmann, K. & Gehren, T. 1988, *A&A*, 199, 269

Hauck, B. & Mermilliod, M. 1998, *A&AS*, 129, 431

Houk, N. 1978, *Michigan catalogue of two dimensional spectral types for the HD stars*, Vol. 2 (Ann Arbor: University of Michigan)

Houk, N. 1982, *Michigan catalogue of two dimensional spectral types for the HD stars*, Vol. 3 (Ann Arbor: University of Michigan)

Houk, N. & Cowley, A. P. 1975, *Michigan catalogue of two dimensional spectral types for the HD stars*, Vol. 1 (Ann Arbor: University of Michigan)

Houk, N. & Smith-Moore, M. 1988, *Michigan catalogue of two dimensional spectral types for the HD stars*, Vol. 4 (Ann Arbor: University of Michigan)

Houk, N. & Swift, C. 1999, *Michigan catalogue of two dimensional spectral types for the HD stars*, Vol. 5 (Ann Arbor: University of Michigan)

Irwin, A. W. 1981, *ApJS*, 45, 621

Johnson, D. R. H. & Soderblom, D. R. 1987, *AJ*, 93, 864

Kaufer, A., Stahl, O., Tubbesing, S., et al. 1999, *The Messenger*, 95, 8

Koch, A. & Edvardsson, B. 2002, *A&A*, 381, 500 (KE02)

Komarovskii, V. A. 1991, *Optika i Spektroskopiya*, 71, 559

Koornneef, J. 1983, *A&AS*, 51, 489

Kupka, F., Piskunov, N., Ryabchikova, T. A., Stempels, H. C., & Weiss, W. W. 1999, *A&AS*, 138, 119

Kurucz, R. L. 1993, *SAO*, Cambridge, CDROM 18

Kurucz, R. L. 1994, *SAO*, Cambridge, CDROM 20–22

Kurucz, R. L. 2003, Home page - line lists (<http://kurucz.harvard.edu/linelists.html>)

Kurucz, R. L., Furenlid, I., Brault, J., & Testerman, L. 1984, *The Solar Flux Atlas from 296 nm to 1300 nm* (National Solar Observatory)

Lawler, J. E., Whaling, W., & Grevesse, N. 1990, *Nature*, 346, 635

Lawler, J. E., Wickliffe, M. E., den Hartog, E. A., & Sneden, C. 2001, *ApJ*, 563, 1075

Learner, R. C. M., Davies, J., & Thorne, A. P. 1991, *MNRAS*, 248, 414

Möller, W., Hühnermann, H., Alkhazov, G., & Panteleev, V. 1993, *Physical Review Letters*, 70, 541

Manfroid, J. & Sterken, C. 1987, *A&AS*, 71, 539

Mashonkina, L. & Gehren, T. 2000, *A&A*, 364, 249

Mashonkina, L. I. 2000, *Astronomy Reports*, 44, 558

Mermilliod, J.-C. 1987, *A&AS*, 71, 413

Meylan, T., Furenlid, I., Wiggs, M. S., & Kurucz, R. L. 1993, *ApJS*, 85, 163

Moore, C. E., Minnaert, M. G. J., & Houtgast, J. 1966, *The solar spectrum 2935 Å to 8770 Å* (Washington: National Bureau of Standards Monograph, US Government Printing Office)

Morell, O., Källander, D., & Butcher, H. R. 1992, *A&A*, 259, 543 (MKB92)

Neckel, H. 1986, *A&A*, 159, 175

Nilsson, H., Zhang, Z. G., Lundberg, H., Johansson, S., & Nordström, B. 2002, *A&A*, 382, 368

Olsen, E. H. 1983, *A&AS*, 54, 55

Olsen, E. H. 1993, *A&AS*, 102, 89

Olsen, E. H. 1994, *A&AS*, 106, 257

Olsen, E. H. & Perry, C. L. 1984, *A&AS*, 56, 229

Pagel, B. E. J. 1989, in *Evolutionary Phenomena in Galaxies*. Edited by J.E. Beckman and B.E.J. Pagel. (Cambridge and New York: Cambridge University Press), 201–223

Perryman, M. A. C., Brown, A. G. A., Lebreton, Y., et al. 1998, *A&A*, 331, 81

Perryman, M. A. C. & ESA. 1997, *The HIPPARCOS and TYCHO catalogues. Astrometric and photometric star catalogues derived from the ESA HIPPARCOS*

Space Astrometry Mission (Noordwijk: ESA Publications Division. Series: ESA SP Series vol no. 1200)

Pfeiffer, B., Kratz, K.-L., & Thielemann, F.-K. 1997, *Z. Phys. A*, Vol. 357, p. 235-238, 357, 235

Pickering, J. C. 1996, *ApJS*, 107, 811

Pickering, J. C. & Thorne, A. P. 1996, *ApJS*, 107, 761

Porto de Mello, G. F., da Silva, L., & de Nader, R. V. 2005, *A&A*, to be submitted

Praderie, F. 1967, *Annales d'Astrophysique*, 30, 31

Schaerer, D., Charbonnel, C., Meynet, G., Maeder, A., & Schaller, G. 1993a, *A&AS*, 102, 339 (Gen92/96)

Schaerer, D., Meynet, G., Maeder, A., & Schaller, G. 1993b, *A&AS*, 98, 523 (Gen92/96)

Schaller, G., Schaerer, D., Meynet, G., & Maeder, A. 1992, *A&AS*, 96, 269 (Gen92/96)

Schuster, W. J., Parrao, L., & Contreras Martinez, M. E. 1993, *A&AS*, 97, 951

Severny, A. B. 1958, *Izv. Krymsk. Astrofiz. Observ.*, 18, 96

Sitterly, C. M. & King, A. S. 1943, *Proc. Am. Phil. Soc.*, 86, 339

Sneden, C., Cowan, J. J., Lawler, J. E., et al. 2002, *ApJ*, 566, L25

Steffen, M. 1985, *A&AS*, 59, 403

Udry, S., Mayor, M., Maurice, E., et al. 1999, in *ASP Conf. Ser. 185: IAU Colloq. 170: Precise Stellar Radial Velocities*, 383

Vidal, C. R., Cooper, J., & Smith, E. W. 1971, *J. Quant. Spec. Radiat. Transf.*, 11, 263

Villemoes, P. & Wang, M. 1994, *Z. Phys. D*, 30, 19

Warren, W. H. & Hoffleit, D. 1987, *BAAS*, 19, 733

Whaling, W. 1983, Technical Report 84 A, Calif. Inst. of Techn., Pasadena

Wickliffe, M. E., Salih, S., & Lawler, J. E. 1994, *Journal of Quantitative Spectroscopy and Radiative Transfer*, 51, 545

Woolf, V. M., Tomkin, J., & Lambert, D. L. 1995, *ApJ*, 453, 660 (WTL95)

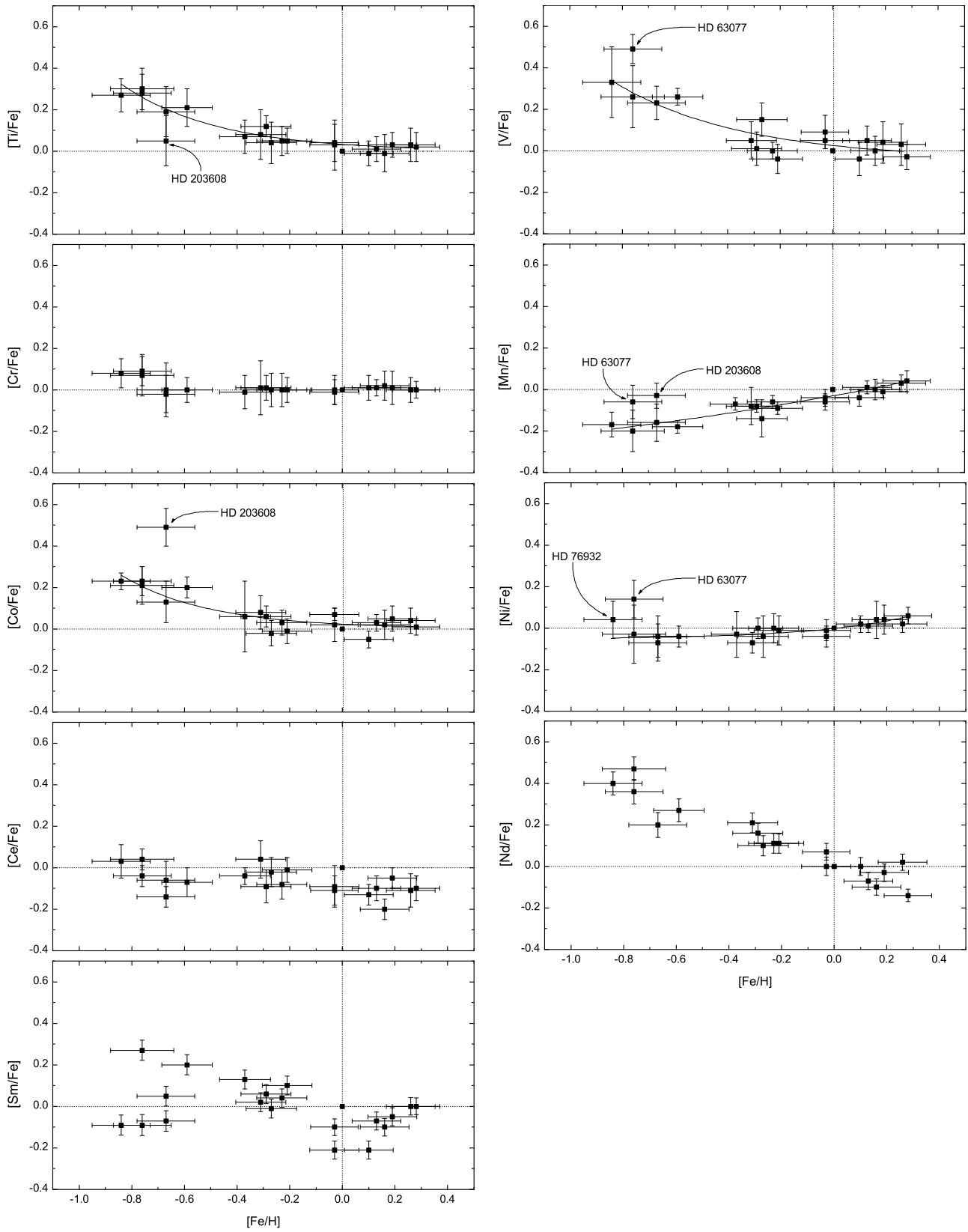


Fig. 12. Abundance patterns for all contaminating elements. Outliers are indicated by arrows labelled with their respective HD numbers. Solid lines, when present, represent exponential fits to the well behaved data points.

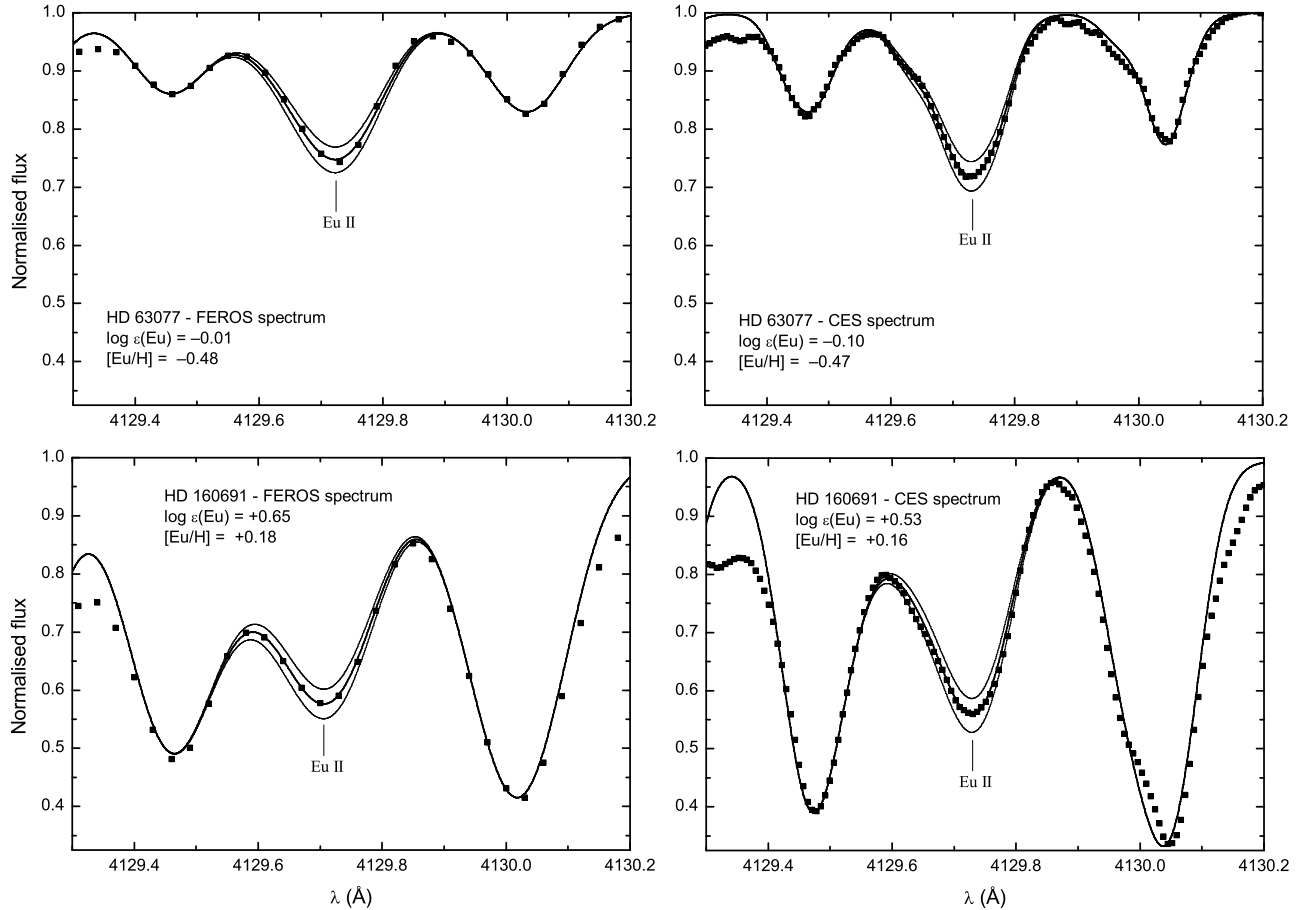


Fig. 14. Examples of spectral syntheses of the Eu II line at 4129.72 Å. FEROS and CES spectra are presented for two stars with extreme Eu abundances (HD 63 077 and HD 160 691). Points are the observed spectra. Thick lines are the best fitting synthetic spectra, calculated with the shown Eu abundances. Thin lines represent variations in the Eu abundance $\Delta \log \varepsilon(\text{Eu}) = \pm 0.05$ dex. The shown abundances are the ones that best fit the presented spectra, and not the average values that are presented in Table 14.

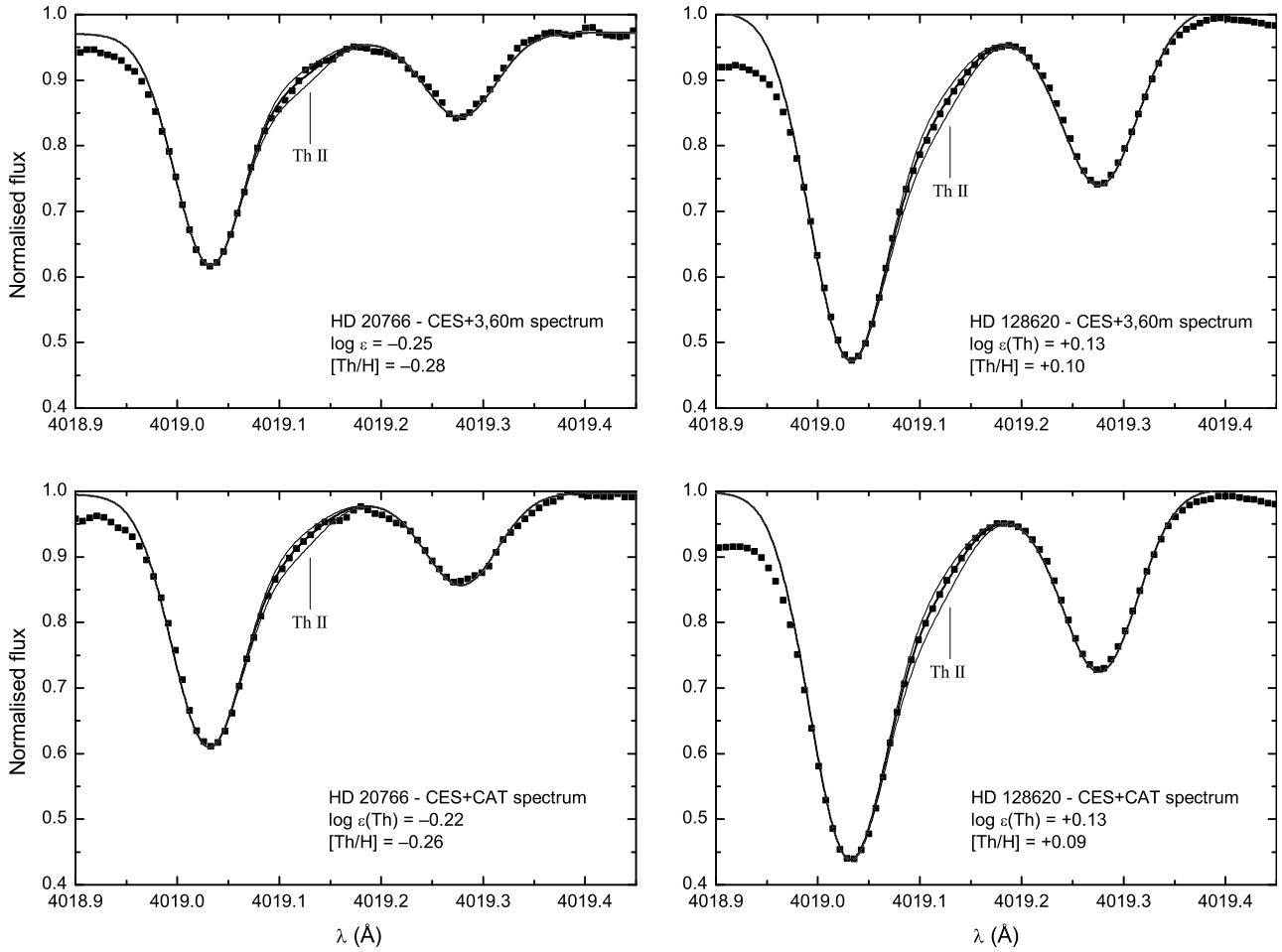


Fig. 19. Examples of spectral syntheses of the Th II line at 4019.13 Å. 3.60 m and CAT spectra are presented for two stars with extreme Th abundances (HD 20766 and HD 128620). Points are the observed spectra. Thick lines are the best fitting synthetic spectra, calculated with the shown Th abundances. Thin lines represent variations in the Th abundance $\Delta \log \varepsilon(\text{Th}) = \pm 0.20$ dex. The shown abundances are the ones that best fit the presented spectra, and not the average values that are presented in Table 14.